

# Bayesian Fully-Connected Tensor Network for Hyperspectral-Multispectral Image Fusion

Linsong Shan, Zecan Yang, Laurence T. Yang, *Fellow, IEEE*, Changlong Li, Honglu Zhao, Xin Nie

**Abstract**—Tensor decomposition is a powerful tool for data analysis and has been extensively employed in the field of hyperspectral-multispectral image fusion (HMF). Existing tensor decomposition-based fusion methods typically rely on disruptive data vectorization/reshaping or impose rigid constraints on the arrangement of factor tensors, hindering the preservation of spatial-spectral structures and the modeling of cross-dimensional correlations. Although recent advances utilizing the Fully-Connected Tensor Network (FCTN) decomposition have partially alleviated these limitations, the process of reorganizing data into higher-order tensors still disrupts the intrinsic spatial-spectral structure. Furthermore, these methods necessitate extensive manual parameter tuning and exhibit limited robustness against noise and spatial degradation. To alleviate these issues, we propose the Bayesian FCTN (BFCTN) method. Within this probabilistic framework, a hierarchical sparse prior that characterizing the sparsity of physical elements, establishes connections between the factor tensors. This framework explicitly models the intrinsic physical coupling among spatial structures, spectral signatures, and local scene homogeneity. For model learning, we develop a parameter estimation method based on Variational Bayesian inference (VB) and the Expectation-Maximization (EM) algorithm, which significantly reduces the need for manual parameter tuning. Extensive experiments demonstrate that BFCTN not only achieves state-of-the-art fusion accuracy and strong robustness but also exhibits practical applicability in complex real-world scenarios. The source code is available at: <https://github.com/LinsongShan/BFCTN>.

**Index Terms**—Image fusion, tensor decomposition, Bayesian learning, fully-connected tensor network

## I. INTRODUCTION

**H**YPERSPECTRAL imaging provides a wealth of spectral data across a contiguous bands, which is vital for precise material identification and classification in diverse applications such as computer vision [36], remote sensing information [21], environmental monitoring [39], and agriculture [38]. However, the acquisition of hyperspectral images (HSI) is constrained by the limitations of the sensor hardware, and the comprehensive spectral information is frequently obtained at the expense of spatial resolution. In contrast, multispectral imaging (MSI) captures fewer spectral bands but generally provides higher

spatial resolution. To leverage the advantages of both imaging modalities, the fusion of HSI and MSI to produce high-resolution hyperspectral images (HR-HSI) with both superior spectral and spatial resolutions has emerged as a central research focus in academia and industry alike [53].

The fusion of hyperspectral and multispectral images has witnessed considerable advancement, driven by advances in diverse methodologies. This research can be classified into three primary approaches: traditional image fusion techniques, deep learning frameworks, and low-rank decomposition strategies.

Traditional image fusion methods provide a basic framework for HMF tasks. Gomez et al. [25] demonstrated that wavelet transforms effectively enhance both spatial and spectral resolutions through resolution analysis. These methods are simple to implement and preserve essential image details. Pan-sharpening [26] further improves hyperspectral images by integrating high-resolution panchromatic and low-resolution spectral data. However, in complex scenes, multi-scale decomposition alone fails to capture the rich spectral information of hyperspectral data.

In recent years, the rise of deep learning has significantly transformed the landscape of image fusion research, enabling automatic extraction of high-level features. In early supervised learning approaches, Wang et al. [28] pioneered the application of CNNs to HMF, while Han et al. [29] achieved multi-scale feature extraction through MSCNN. Xiao et al. [30] proposed a GAN framework further optimized distribution alignment via adversarial training. Dian et al. [56], [57] extended this direction with model-guided and low-rank deep frameworks for spectral super-resolution, effectively integrating spatial-spectral priors. More recently, Liu et al. [45] proposed a novel low-rank Transformer architecture that enhances high-resolution imaging through attention mechanisms. To address the dependency on annotated data in supervised learning, Dian et al. [42] developed a zero-shot learning framework, while the teams of Wang [55] and Li [43], [44] established new paradigms through unsupervised Tucker decomposition and enhanced image prior methods, respectively, eliminating the need for supervised data. In addition, Cao et al. [58], [59] proposed hybrid Transformer architectures for blind hyperspectral-multispectral fusion, further improving robustness in unsupervised settings. Despite these advancements significantly improving practical applicability, challenges such as model interpretability [32] and stable generalization across diverse scenarios remain areas for further research, driving the field toward more robust and transparent solutions.

Low-rank decomposition-based image fusion methods leverage the intrinsic low-rank property of images, employing

**Linsong Shan, Changlong Li and Honglu Zhao** are with the School of Computer Science and Technology, Huazhong University of Science and Technology, Wuhan, 430074, China. **Laurence T. Yang** is with the School of Computer Science and Technology, Huazhong University of Science and Technology, Wuhan 430074, China, also with the School of Computer Science and Artificial Intelligence, Zhengzhou University, Zhengzhou 450001, China, and also with the Department of Computer Science, St. Francis Xavier University, Antigonish, NS B2G 2W5, Canada. **Zecan Yang** and **Xin Nie** are with the School of Computer Science and Artificial Intelligence, Zhengzhou University, Zhengzhou 450001, China. E-mail: {[shanlinsong6](mailto:shanlinsong6@hust.edu.cn), [ltyang](mailto:ltyang@hust.edu.cn), [zecanyang](mailto:zecanyang@hust.edu.cn), [aria.hl.zhao](mailto:aria.hl.zhao@gmail.com)}@gmail.com, [changlongli@hust.edu.cn](mailto:changlongli@hust.edu.cn), [niefllhx@foxmail.com](mailto:niefllhx@foxmail.com);

matrix or tensor decomposition techniques to construct unified models that embed multi-source data into a common low-rank representation, thereby achieving effective HMF. Operating in an unsupervised manner without requiring training data, these approaches demonstrate strong adaptability and broad applicability. In early research, Yokoya et al. [1] proposed the CNMF method which effectively preserves spectral-spatial consistency through non-negative matrix factorization, while Simoes et al. [41] developed the Hysure algorithm utilizing subspace regularization for smooth alignment. However, conventional matrix decomposition methods face limitations in capturing high-order correlations in complex scenes and exhibit sensitivity to noise. In contrast, tensor decomposition provides more effective representation of high-dimensional data [49]–[51]. As natural tensors, hyperspectral images have motivated numerous tensor-based fusion methods. Notable examples include CSTF [5], which adopts coupled tensor factorization, and NLSTF [3], [4], which incorporates non-local similarity. A series of groundbreaking works, such as LTTR [6], LTMR [7], and GTNN [40], further advance this line of research. More recently, CTDF [19] introduces a fourth-order spatial decomposition scheme. Furthermore, JSSO [46] achieves significant improvements in spatial detail reconstruction via joint spatial-spectral optimization. BGS-GTF [47], establishes a more generalizable tensor fusion framework capable of handling diverse blurring scenarios.

HMF tasks face challenges such as noise interference, low resolution, and complex spectral–spatial correlations. Bayesian methods show strong potential by naturally incorporating prior knowledge [48], handling noise and missing data, and adaptively adjusting parameters. When combined with tensor decomposition, they can model complex high-dimensional structures with solid theoretical foundations [15]. As a result, Bayesian tensor decomposition has proven effective for improving HMF performance. Representative approaches include Bayesian CP [10], t-SVD [33], and tensor ring (TR) decomposition [34]. Recently, Zheng et al. [8] proposed a FCTN decomposition to capture intrinsic correlations and permutation invariance across tensor modes. Compared with CP and Tucker, FCTN better models high-order interactions and overcomes TR/TT sensitivity to mode arrangements. Jin et al. [18] further developed a higher-order coupled FCTN for hyperspectral super-resolution, achieving improved resolution and representation. However, its step-up operation distorts the image structure, and the traditional optimization process requires heavy computation and parameter tuning, limiting generalization.

In this paper, we propose a novel Bayesian Fully-Connected Tensor Network for HMF tasks. The main contributions of our work can be summarized as:

- This paper introduces the first integration of Bayesian learning with FCTN decomposition in HMF tasks. The employment of hierarchical sparse priors for the construction of a fully connected tensor network between factor tensors is a novel aspect of this model, which allows flexible cross-dimensional tensor relations and thus better captures low-rank structures and data correlations.
- A parameter estimation method integrating VB and EM is

proposed, effectively addressing non-convex optimization challenges in HMF tasks while streamlining parameter selection. This approach systematically mitigates uncertainties induced by manual parameter tuning.

- Multi-scenario experiments prove that BFCTN achieves state-of-the-art fusion performance across multiple datasets. Its flexible low-rank modeling capability effectively addresses spatial degradation discrepancies and strong noise interference, while maintaining exceptional robustness and applicability in real-world scenarios.

The remainder of this paper is organized as follows. Section II introduces the notation and defines the fusion problem. Section III describes the proposed BFCTN with its prior settings and posterior inference. Section IV reports experimental results and analysis. Section V concludes the paper.

## II. PRELIMINARIES AND PROBLEM FORMULATION

### A. Notations and Preliminaries

Tensor is an  $n$ -dimensional array ( $n \geq 3$ ) that serves as a versatile framework for modeling and analyzing multidimensional data. In this article, we adopt lowercase letters, bold lowercase letters, bold uppercase letters, and calligraphic letters to represent scalars, vectors, matrices, and tensors, respectively (e.g.,  $z$ ,  $\mathbf{z}$ ,  $\mathbf{Z}$ ,  $\mathcal{Z}$ ). Additionally, given an  $N$ -th order tensor  $\mathcal{Z} \in \mathbb{R}^{I_1 \times I_2 \times \dots \times I_N}$ ,  $\mathcal{Z}(i_1, i_2, \dots, i_N)$  or  $z_{i_1, i_2, \dots, i_N}$  represents its  $(i_1, i_2, \dots, i_N)$ -th element,  $\mathbf{Z}_{(n)}$  represents its mode- $n$  unfolding,  $\text{vec}(\cdot)$  represents its vectorization, and the Frobenius norm is represented as  $\|\mathcal{Z}\|_F$ .

FCTN decomposition is the cornerstone of the proposed method. In accordance with the findings of [8], the element-wise form of FCTN decomposition is as follows:

$$\begin{aligned} \mathcal{Z}(i_1, \dots, i_N) = & \sum_{r_{1,2}}^{R_{1,2}} \dots \sum_{r_{1,N}}^{R_{1,N}} \sum_{r_{2,3}}^{R_{2,3}} \dots \sum_{r_{2,N}}^{R_{2,N}} \dots \sum_{r_{N-1,N}}^{R_{N-1,N}} \\ & \{ \mathcal{T}_1(i_1, r_{1,2}, r_{1,3}, \dots, r_{1,N}) \\ & \mathcal{T}_2(r_{1,2}, i_2, r_{2,3}, \dots, r_{2,N}) \dots \\ & \mathcal{T}_n(r_{1,n}, \dots, r_{n-1,n}, i_n, r_{n,n+1}, \dots, r_{n,N}) \dots \\ & \mathcal{T}_N(r_{1,N}, r_{2,N}, \dots, r_{N-1,N}, i_N) \}, \end{aligned} \quad (1)$$

where  $\{\mathcal{T}_n\}_{n=1}^N$  represents the factor tensors,  $i_n$  corresponds to the  $N$  dimensions of the original tensor, and  $(R_{1,2}, \dots, R_{1,N}, \dots, R_{N-1,N})$  represents the FCTN-ranks. It can be seen that FCTN decomposition decomposes an  $N$ -th order tensor into  $N$   $N$ -th order tensors, with its simplified representation as  $\mathcal{Z} = \text{FCTN}(\{\mathcal{T}_n\}_{n=1}^N)$ .

Notably, the mode product of tensors plays a significant role in this study. Assuming the  $n$ -mode product of a tensor  $\mathcal{Z}$  and a matrix  $\mathbf{P}$  is denoted as  $\mathcal{Z} \times_n \mathbf{P}$ , the following equation can be derived based on the properties of FCTN:

$$\mathcal{Z} \times_n \mathbf{P} \Leftrightarrow \text{FCTN}(\mathcal{T}_1, \mathcal{T}_2, \dots, \mathcal{T}_n \times \mathbf{P}, \dots, \mathcal{T}_N). \quad (2)$$

Furthermore, the composition of FCTN is of considerable significance. Its expression is  $\text{FCTN}(\{\mathcal{T}_n\}_{n=1}^N) = \mathcal{Z}$ . It

should be noted that, in certain cases, it is necessary to isolate a specific factor tensor. The composition of  $\{\mathcal{T}_n\}_{n=1}^N$  without  $\mathcal{T}_n$  defined to be  $\mathcal{Z}_{\neq n}$ , assuming  $\mathcal{Z}_{\neq n} = \text{FCTN}(\{\mathcal{T}_n\}_{n=1}^N/\mathcal{T}_n)$ , the mode- $n$  unfolding of the tensor  $\mathcal{Z}$  can be expressed as

$$\mathbf{Z}_{(n)} = (\mathbf{T}_n)_{(n)} (\mathbf{Z}_{\neq n})_{[m_{1:N-1}; n_{1:N-1}]}, \quad (3)$$

where

$$m_i = \begin{cases} 2i, & \text{if } i < n, \\ 2i - 1, & \text{if } i \geq n, \end{cases} \text{ and } n_i = \begin{cases} 2i - 1, & \text{if } i < n, \\ 2i, & \text{if } i \geq n, \end{cases}$$

$(\mathbf{T}_n)_{(n)}$  represents the mode- $n$  unfolding of  $\mathcal{T}_n$ , and  $(\mathbf{Z}_{\neq n})_{[m_{1:N-1}; n_{1:N-1}]}$  represents the mode- $n$  unfolding of the synthesis of other factors. This expansion method is derived from the definition of FCTN decomposition [8].

### B. Problem Formulation

With regard to the HMF tasks, the observed images, including low-resolution hyperspectral images (LR-HSI) and high-resolution multispectral images (HR-MSI) are regarded as degraded components of the reference images (HR-HSI). The objective of our study is to restore the reference image by decomposing these degraded components and exploring their low-rank structure.

The reference image is denoted as  $\mathcal{Z} \in \mathbb{R}^{W \times H \times S}$ , where  $W$  and  $H$  represent the image width and height, respectively, and  $S$  represents the number of spectral channels. Additionally, the LR-HSI and HR-MSI are denoted as  $\mathcal{H} \in \mathbb{R}^{w \times h \times S}$  and  $\mathcal{M} \in \mathbb{R}^{W \times H \times s}$ . The degradation relationship between the observed images and the reference image is as follows:

$$\begin{aligned} \mathcal{H} &= \mathcal{Z} \times_1 \mathbf{P}_1 \times_2 \mathbf{P}_2 + \mathcal{N}_h \\ \mathcal{M} &= \mathcal{Z} \times_3 \mathbf{P}_3 + \mathcal{N}_m, \end{aligned} \quad (4)$$

where,  $\mathbf{P}_1$  and  $\mathbf{P}_2$  are the spatial degradation factors corresponding to width and height, respectively, and  $\mathbf{P}_3$  is the spectral degradation factor. The  $\mathcal{N}_h$  and  $\mathcal{N}_m$  represent distinct noise interference components. With the degradation model above, the HMF tasks is expressed as minimizing the following optimization function:

$$\min_{\mathcal{Z}} \|\mathcal{H} - \mathcal{Z} \times_1 \mathbf{P}_1 \times_2 \mathbf{P}_2\|_{\text{F}}^2 + \eta \|\mathcal{M} - \mathcal{Z} \times_3 \mathbf{P}_3\|_{\text{F}}^2, \quad (5)$$

where  $\eta$  is a hyperparameter employed to balance the influence of  $\mathcal{H}$  and  $\mathcal{M}$ .

The potential lower-rank structure better accentuates the advantages of FCTN decomposition. Therefore, we assume the reference image  $\mathcal{Z} \in \mathbb{R}^{W \times H \times S}$  is chunked into overlapping patches of size  $I_1 \times I_2 \times I_3$  with overlap size  $p$ . Since the observed LR-HSI  $\mathcal{H} \in \mathbb{R}^{w \times h \times S}$  is obtained by spatially downsampling  $\mathcal{Z}$  by a factor of  $sf$ , it is chunked into patches of size  $I'_1 \times I'_2 \times I_3$ , where the spatial dimensions satisfy  $I_1/I'_1 = W/w = I_2/I'_2 = H/h = sf$ . Similarly, the observed HR-MSI  $\mathcal{M} \in \mathbb{R}^{W \times H \times s}$  is spectrally degraded from  $\mathcal{Z}$ , and is thus chunked into patches of size  $I_1 \times I_2 \times I'_3$ , where  $I_3/I'_3 = S/s$ . Subsequently, the image patches are classified into  $K$  groups in accordance with the columns of their original positions, with  $I_4$  representing the number of

image patches in this group. As a result,  $K$  groups of LR-HSI and HR-MSI image patches are generated, with each group denoted by  $\mathcal{H}^k \in \mathbb{R}^{I'_1 \times I'_2 \times I_3 \times I_4}$  and  $\mathcal{M}^k \in \mathbb{R}^{I_1 \times I_2 \times I'_3 \times I_4}$ . The corresponding reference image patch is represented as  $\mathcal{Z}^k \in \mathbb{R}^{I_1 \times I_2 \times I_3 \times I_4}$ . Additionally, the relationship between  $\mathcal{H}^k$ ,  $\mathcal{M}^k$  and  $\mathcal{Z}^k$  still satisfy Eq. (4). While chunking the observed image into overlapping patches increases computational costs, it facilitates more effective feature extraction. This group-wise strategy avoids explicitly modeling the spatial arrangement of patches, thus preventing the computational need to construct tensors of even higher order.

The standard FCTN models a tensor  $\mathcal{Z}$  as the product of multiple factor components across  $N$  modes. However, in the HMF task, decomposing the spectral tensor into an excessively high-order structure may disrupt the inherent spatial-spectral correlations, thereby reducing physical interpretability and robustness under complex degradations. Therefore, the number of factor tensors is restricted to four, corresponding to the observed 4th-order tensorized image. Fig. 1 shows the structure of the FCTN decomposition and its 4th-order graphical representation. In addition, the FCTN decomposition of  $\mathcal{Z}^k$  can be denoted as

$$\mathcal{Z}^k = \text{FCTN}(\mathcal{T}_1^k, \mathcal{T}_2^k, \mathcal{T}_3^k, \mathcal{T}_4^k), \quad (6)$$

where  $\mathcal{T}_1^k \in \mathbb{R}^{I_1 \times R_{1,2} \times R_{1,3} \times R_{1,4}}$ ,  $\mathcal{T}_2^k \in \mathbb{R}^{R_{1,2} \times I_2 \times R_{2,3} \times R_{2,4}}$ ,  $\mathcal{T}_3^k \in \mathbb{R}^{R_{1,3} \times R_{2,3} \times I_3 \times R_{3,4}}$ ,  $\mathcal{T}_4^k \in \mathbb{R}^{R_{1,4} \times R_{2,4} \times R_{3,4} \times I_4}$  are factor tensors, and  $\{R_{n_1, n_2}\}_{1 \leq n_1 < n_2 \leq 4}$  is FCTN ranks.

Based on Eq. (2) and Eq. (4), the image patches  $\mathcal{H}^k$  and  $\mathcal{M}^k$  can be expressed in terms of factor tensors as

$$\begin{aligned} \mathcal{H}^k &= \text{FCTN}(\mathcal{T}_1^k \times_1 \mathbf{P}_1, \mathcal{T}_2^k \times_2 \mathbf{P}_2, \mathcal{T}_3^k, \mathcal{T}_4^k) \\ \mathcal{M}^k &= \text{FCTN}(\mathcal{T}_1^k, \mathcal{T}_2^k, \mathcal{T}_3^k \times_3 \mathbf{P}_3, \mathcal{T}_4^k). \end{aligned} \quad (7)$$

With the above considerations, the optimization function in Eq. (5) can be rewritten as follows:

$$\begin{aligned} \min_{\{\mathcal{T}_n^k\}_{n=1}^4} & \|\mathcal{H}_k - \text{FCTN}(\mathcal{T}_1^k \times_1 \mathbf{P}_1, \mathcal{T}_2^k \times_2 \mathbf{P}_2, \mathcal{T}_3^k, \mathcal{T}_4^k)\|_{\text{F}}^2 \\ & + \eta \|\mathcal{M}_k - \text{FCTN}(\mathcal{T}_1^k, \mathcal{T}_2^k, \mathcal{T}_3^k \times_3 \mathbf{P}_3, \mathcal{T}_4^k)\|_{\text{F}}^2. \end{aligned} \quad (8)$$

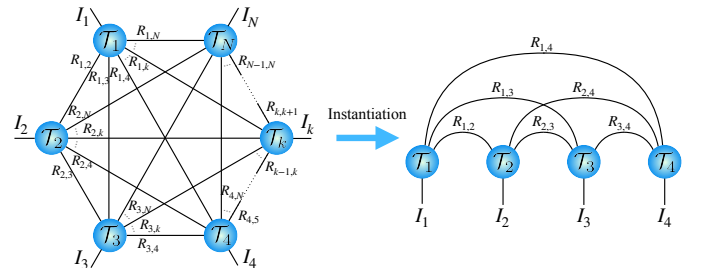


Fig. 1: Graphical representation of FCTN decomposition and its 4th-order instantiation.

### III. MODEL DESCRIPTION

This section will present the proposed model in the form of a probabilistic graphical model. The model can be summarised in terms of two principal components: the model priors setting and the model inference.

$$p\left(\mathcal{H}^k \mid \{\mathcal{T}_n^k\}_{n=1}^4, \tau_h^k\right) = \prod_{i'_1=1}^{I'_1} \prod_{i'_2=1}^{I'_2} \prod_{i'_3=1}^{I'_3} \prod_{i'_4=1}^{I'_4} \mathcal{N}\left(h_{i'_1 i'_2 i'_3 i'_4}^k \mid \text{FCTN}\left(\mathcal{T}_1^k \times_1 \mathbf{P}_1, \mathcal{T}_2^k \times_2 \mathbf{P}_2, \mathcal{T}_3^k, \mathcal{T}_4^k\right)_{i'_1 i'_2 i'_3 i'_4}, \tau_h^{k-1}\right) \quad (9)$$

$$p\left(\mathcal{M}^k \mid \{\mathcal{T}_n^k\}_{n=1}^4, \tau_m^k\right) = \prod_{i_1=1}^{I_1} \prod_{i_2=1}^{I_2} \prod_{i'_3=1}^{I'_3} \prod_{i_4=1}^{I_4} \mathcal{N}\left(m_{i_1 i_2 i'_3 i_4}^k \mid \text{FCTN}\left(\mathcal{T}_1^k, \mathcal{T}_2^k, \mathcal{T}_3^k \times_3 \mathbf{P}_3, \mathcal{T}_4^k\right)_{i_1 i_2 i'_3 i_4}, \tau_m^{k-1}\right) \quad (10)$$

### A. Model Prior Setting

Initially, the prior distributions for the observed image patches, designated as  $\mathcal{H}^k$  and  $\mathcal{M}^k$ , are defined to follow multivariate normal distribution. By means of Eq. (7), the mean of the prior distribution for  $\mathcal{H}^k$  can be expressed in terms of the factor tensors and degradation factors  $\mathbf{P}_1$  and  $\mathbf{P}_2$  through the FCTN operation. Similarly, the mean of the prior distribution for  $\mathcal{M}^k$  can be described by the factor tensors and degradation factor  $\mathbf{P}_3$ . Moreover, the noise precision parameters for the prior distributions of  $\mathcal{H}^k$  and  $\mathcal{M}^k$  are represented by  $\tau_h^k$  and  $\tau_m^k$ , respectively. Therefore, the prior distributions of  $\mathcal{H}^k$  and  $\mathcal{M}^k$  are given in Eq. (9) and Eq. (10).

1) *Latent Factor Tensors with Its Hyperprior*: Due to the strong correlations among factor tensors in FCTN decomposition, it is imperative that the prior settings of the factors are designed to ensure their independence and structural integrity. Hence, we assume each factor tensor  $\mathcal{T}_n^k$  follows a tensor normal distribution [14] with a mean of zero and a covariance determined by a set of matrices. The prior distribution for factor tensor is represented as

$$\begin{aligned} p\left(\mathcal{T}_n^k \mid \boldsymbol{\lambda}_{1,n}^k, \dots, \boldsymbol{\lambda}_{n-1,n}^k, \boldsymbol{\lambda}_{n,n+1}^k, \dots, \boldsymbol{\lambda}_{n,N}^k\right) \\ = \prod_{i_n}^{I_n} \mathcal{TN}\left(\mathcal{T}_n^k(i_n) \mid \mathbf{0}, \boldsymbol{\Lambda}_{1,n}^k, \dots, \boldsymbol{\Lambda}_{n-1,n}^k, \boldsymbol{\Lambda}_{n,n+1}^k, \dots, \boldsymbol{\Lambda}_{n,N}^k\right), \end{aligned} \quad (11)$$

where  $\boldsymbol{\Lambda}_{n_1, n_2}^k = \text{diag}(\boldsymbol{\lambda}_{n_1, n_2}^k)$ ,  $\text{diag}(\cdot)$  denotes the matrixization of a vector and  $\mathcal{TN}(\cdot)$  denotes tensor normal distribution. The  $\boldsymbol{\lambda}_{n_1, n_2}^k$  is a parameter to establish a connection between the factor tensors  $\mathcal{T}_{n_1}^k$  and  $\mathcal{T}_{n_2}^k$ .

The structure of the covariance of the above distribution is complex and non-intuitive. Fortunately, with the rule of linear transformation from tensor normal distribution to multivariate normal distribution<sup>1</sup>, this covariance can be replaced by the matricization for the Kronecker product of a set of vectors. Thus, the prior distribution can be expressed as a more intuitive multivariate normal distribution as follows:

$$\begin{aligned} p\left(\mathcal{T}_n^k \mid \boldsymbol{\lambda}_{1,n}^k, \dots, \boldsymbol{\lambda}_{n-1,n}^k, \boldsymbol{\lambda}_{n,n+1}^k, \dots, \boldsymbol{\lambda}_{n,N}^k\right) \\ = \prod_{i_n}^{I_n} \mathcal{N}\left(\mathbf{T}_{n(n)}^k(i_n) \mid \mathbf{0}, \boldsymbol{\Lambda}_n^k\right), \end{aligned} \quad (12)$$

where  $\boldsymbol{\Lambda}_n^k = \text{diag}(\boldsymbol{\lambda}_{n,N}^k \otimes \dots \otimes \boldsymbol{\lambda}_{n,n+1}^k \otimes \boldsymbol{\lambda}_{n,n-1}^k \otimes \dots \otimes \boldsymbol{\lambda}_{1,n}^k)$ .

With the above, each pair of factor tensors  $\mathcal{T}_{n_1}^k$  and  $\mathcal{T}_{n_2}^k$  are interconnected by  $\boldsymbol{\lambda}_{n_1, n_2}^k$ , adhering strictly to the FCTN

<sup>1</sup> $\mathcal{X} \sim \mathcal{TN}(\mathcal{M}, \Sigma_1, \Sigma_2, \dots, \Sigma_k) \Leftrightarrow \text{vec}(\mathcal{X}) \sim \mathcal{N}(\text{vec}(\mathcal{M}), \Sigma_k \otimes \Sigma_{k-1} \otimes \dots \otimes \Sigma_1)$  [9].

decomposition paradigm and forming a fully connected tensor network. The parameter  $\boldsymbol{\lambda}_{n_1, n_2}^k$  for establishing the connection of factors is considered to follow a Gamma distribution, as

$$p\left(\boldsymbol{\lambda}_{n_1, n_2}^k\right) = \prod_r^{R_{n_1, n_2}} \text{Ga}\left((\boldsymbol{\lambda}_{n_1, n_2}^k)_r \mid a_0, b_0\right), \quad (13)$$

where  $\text{Ga}(x \mid a, b) = \frac{b^a x^{a-1} e^{-bx}}{\Gamma(a)}$  represents the expression for the Gamma distribution and  $\mathbb{E}(x) = \frac{a}{b}$ , the  $a_0$  and  $b_0$  represent shape and rate parameters, respectively. The Gamma prior is defined on the positive real domain, aligning with the role of  $\boldsymbol{\lambda}_{n_1, n_2}^k$  as a non-negative association control parameter between factor tensors. Moreover, it allows conjugate updates within the exponential family, which facilitates efficient inference [54].

2) *Precision Parameters*: To ensure the proposed model within a fully Bayesian framework and improve its robustness, the precision parameters  $\tau_h^k$  and  $\tau_m^k$  in Eq. (9) and Eq. (10) are also assumed to follow a Gamma distribution, as

$$p(\tau_h^k) = \text{Ga}(\tau_h^k \mid c_0, d_0), \quad (14)$$

$$p(\tau_m^k) = \text{Ga}(\tau_m^k \mid e_0, f_0). \quad (15)$$

Here,  $c_0$  and  $e_0$  are the shape parameters for these distributions, and  $d_0$  and  $f_0$  are the rate parameters. At this point, a fully Bayesian FCTN model for hyperspectral-multispectral image fusion has been formulated, with the probabilistic graph model presented in Fig. 2.

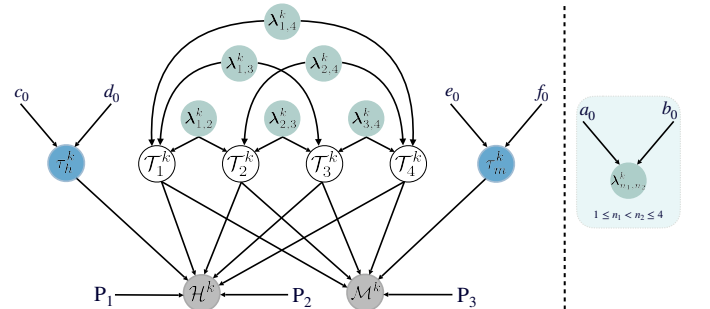


Fig. 2: The probabilistic graphical model of the proposed BFCTN model. The left part is the overall framework of the probabilistic graphical model, and the right part is the details of the hyperparameters of the factor tensors.

3) *Joint Distribution*: To simplify the representation, we use a set to represent all latent variables and hyperparameters in our proposed model, which is designated  $\Xi = \left\{ \{\mathcal{T}_n^k\}_{n=1}^4, \{\lambda_{n_1, n_2}^k\}_{1 \leq n_1 < n_2 \leq 4}, \tau_h^k, \tau_m^k \right\}$ . As illustrated in the probabilistic graphical models in Fig. 2, the joint distribution of the BFCTN model can be written as

$$p(\Xi^k) = p(\mathcal{H}^k | \{\mathcal{T}_n^k\}_{n=1}^4, \tau_h^k) p(\mathcal{M}^k | \{\mathcal{T}_n^k\}_{n=1}^4, \tau_m^k) \prod_{n=1}^4 p(\mathcal{T}_n^k | \lambda_{1,n}^k, \dots, \lambda_{n-1,n}^k, \lambda_{n,n+1}^k, \dots, \lambda_{n,N}^k) \prod_{n_1=1}^3 \prod_{n_2=2}^4 p(\lambda_{n_1, n_2}^k) p(\tau_h^k) p(\tau_m^k). \quad (16)$$

By combining the likelihood terms in Eq. (9) and Eq. (10), the priors of factor tensors and their covariance (given in Eq. (12) and Eq. (13)), and the hyperpriors of the noise precision parameter (described in Eq. (14) and Eq. (15)), the log form of the joint distribution can be expressed as follows:

$$\begin{aligned} \ell(\Xi^k) = & -\frac{\tau_h^k}{2} \|\mathcal{H}^k - \text{FCTN}(\mathcal{T}_1^k \times_1 \mathbf{P}_1, \mathcal{T}_2^k \times_2 \mathbf{P}_2, \mathcal{T}_3^k, \mathcal{T}_4^k)\|_{\text{F}}^2 \\ & -\frac{\tau_m^k}{2} \|\mathcal{M}^k - \text{FCTN}(\mathcal{T}_1^k, \mathcal{T}_2^k, \mathcal{T}_3^k \times_3 \mathbf{P}_3, \mathcal{T}_4^k)\|_{\text{F}}^2 \\ & + \sum_{n=1}^4 \sum_{i_n}^{I_n} \left( \frac{1}{2} \ln |\Lambda_n^k| - \frac{1}{2} \mathbf{T}_n^k(i_n)^\top \Lambda_n^k \mathbf{T}_n^k(i_n) \right) \\ & + \sum_{n_1=1}^3 \sum_{n_2=2}^4 \sum_r^{R_{n_1, n_2}} (a_0 - 1) \ln(\lambda_{n_1, n_2}^k)_r \\ & - \sum_{n_1=1}^3 \sum_{n_2=2}^4 \sum_r^{R_{n_1, n_2}} b_0(\lambda_{n_1, n_2}^k)_r \\ & + \left( \frac{I_1' I_2' I_3' I_4}{2} + c_0 - 1 \right) \ln \tau_h^k \\ & + \left( \frac{I_1 I_2 I_3' I_4}{2} + e_0 - 1 \right) \ln \tau_m^k \\ & - d_0 \tau_h^k - f_0 \tau_m^k + C. \end{aligned} \quad (17)$$

Here,  $C$  is a constant.

## B. Model Inference

This section presents a comprehensive account of the model inference process. The principal objective of our model is to estimate the latent factor tensors  $\{\mathcal{T}_n^k\}_{n=1}^4$  to reconstruct the fused HR-HSI patches. To achieve this objective, the estimation of the parameters  $\{\lambda_{n_1, n_2}^k\}_{1 \leq n_1 < n_2 \leq 4}$  and noise precision parameters  $\tau_h^k$  and  $\tau_m^k$  are equally crucial.

Exact Bayesian inference, despite providing theoretically optimal probability estimates, is often computationally unfeasible in practice, especially for high-order observed data and complex models. Fortunately, variational Bayesian approaches provide an efficient approximate solution [13], [15], [16]. In variational inference, a more tractable distribution is employed

to approximate the complex and intractable posterior distribution, with the Kullback-Leibler (KL) divergence utilized to quantify the divergence between the two distributions.

Therefore, we seek to approximate the true posterior distribution  $p(\Xi^k | \mathcal{H}^k, \mathcal{M}^k)$  in our model by finding a tractable distribution  $q(\Xi^k)$  through the minimization of the KL divergence, that is

$$\begin{aligned} \text{KL}(q(\Xi^k) \| p(\Xi^k | \mathcal{H}^k, \mathcal{M}^k)) = & \ln(p(\mathcal{H}^k, \mathcal{M}^k)) \\ & - \left( \mathbb{E}_{q(\Xi^k)} \left[ \ln p(\Xi^k, \mathcal{H}^k, \mathcal{M}^k) \right] - \mathbb{E}_{q(\Xi^k)} \left[ \ln q(\Xi^k) \right] \right), \end{aligned} \quad (18)$$

where the term  $\ln(p(\mathcal{H}^k, \mathcal{M}^k))$  is a constant, representing the model evidence,  $\mathbb{E}_{q(\Xi^k)}[\ln p(\Xi^k, \mathcal{H}^k, \mathcal{M}^k)] - \mathbb{E}_{q(\Xi^k)}[\ln q(\Xi^k)]$  is called evidence lower bound (ELBO), and due to the non-negative nature of KL divergence, KL divergence will approach 0 when ELBO reaches the bound of evidence.

Based on the mean-field approximation assumption, all latent variables in  $\Xi^k$  can be considered independent of each other, allowing the variational distribution to be factorized as

$$q(\Xi^k) = \prod_{n=1}^4 q(\mathcal{T}_n^k) \prod_{n_1=1}^3 \prod_{n_2=2}^4 q(\lambda_{n_1, n_2}^k) q(\tau_h^k) q(\tau_m^k). \quad (19)$$

With this, the optimal form for each latent variable can be obtained from

$$\ln q_i(\Xi_i^k) = \mathbb{E}_{q(\Xi^k \setminus \Xi_i^k)} \left[ \ln p(\mathcal{H}^k, \mathcal{M}^k, \Xi^k) \right] + C, \quad (20)$$

where  $q_i(\Xi_i^k)$  denotes the estimated posterior distribution of the  $i$ -th variable in  $\Xi$ , and  $\mathbb{E}_{q(\Xi^k \setminus \Xi_i^k)}$  denotes the expectation over the distribution of all variables except for the  $i$ -th variable. Since the prior distributions of all latent variables in the above are drawn from the exponential family, we can derive the posterior distribution for each variable from Eq. (20).

1) *Estimation of Latent Factor Tensors*: As shown in Fig. 2, the latent factor tensor  $\mathcal{T}_n^k$  receives the messages from the observed image patches  $\mathcal{H}^k$  and  $\mathcal{M}^k$ , and its co-parents, including the covariance of all factor tensors. With the Eq. (20), the posterior distribution of  $\mathcal{T}_n^k$  can be constructed by the likelihood terms in Eq. (9)-(10), and the prior in Eq. (12).

However, the difference in dimensions between image patches  $\mathcal{H}^k$  and  $\mathcal{M}^k$  presents a challenge in factoring the latent factor tensors into independent variables. Fortunately, with appropriate regularization [11], the  $\mathcal{T}_n^k$  can be constrained by applying a Dirac delta function, resulting in  $Q(\mathcal{T}_n^k) = \delta(\mathcal{T}_n^k - \hat{\mathcal{T}}_n^k)$  as the point estimate. This allows the variational problem of minimizing the KL divergence to be transformed into an expectation-maximization problem, as follows

$$\hat{\mathcal{T}}_n^{k*} = \arg \max_{\mathbb{E}_{\Pi_{\Xi_i \neq \mathcal{T}_n^k}} Q(\Xi_i)} [\ln p(\Xi^k)]. \quad (21)$$

The EM algorithm can be employed to treat the latent factor tensor as a global variable [10], [12], with the remaining variables designated as latent parameters. This allows for the alternation of updates to each latent factor tensor. Taking  $\mathcal{T}_1^k$

as an example, its point estimate can be viewed as the result of optimizing the following convex function:

$$\begin{aligned} & \max \mathbb{E}_{q(\Xi^k \setminus \mathcal{T}_1^k)} \\ & \left\{ -\frac{\tau_h^k}{2} \|\mathcal{H}^k - \text{FCTN}(\mathcal{T}_1^k \times_1 \mathbf{P}_1, \mathcal{T}_2^k \times_2 \mathbf{P}_2, \mathcal{T}_3^k, \mathcal{T}_4^k)\|_F^2 \right. \\ & -\frac{\tau_m^k}{2} \|\mathcal{M}^k - \text{FCTN}(\mathcal{T}_1^k, \mathcal{T}_2^k, \mathcal{T}_3^k \times_3 \mathbf{P}_3, \mathcal{T}_4^k)\|_F^2 \\ & \left. -\frac{1}{2} \text{Tr} \left( \mathbf{T}_{1(1)}^k \mathbf{\Lambda}_1^k \mathbf{T}_{1(1)}^{k \top} \right) \right\}. \end{aligned} \quad (22)$$

By optimizing the convex function in Eq. (22), we can obtain a Sylvester equation<sup>2</sup> as follows:

$$\begin{aligned} & \mathbf{T}_{1(1)}^k \left\{ \mathbb{E}[\tau_m^k] \mathbb{E} \left[ \mathbf{M}_{\neq 1}^k \mathbf{T}_{\neq 1}^k \right] + \mathbb{E} \left[ \mathbf{\Lambda}_1^k \right] \right\} \\ & + \mathbb{E}[\tau_h^k] \mathbf{P}_1 \mathbf{T}_{1(1)}^k \mathbb{E} \left[ \mathbf{H}_{\neq 1}^k \right] \\ & = \mathbb{E}[\tau_m^k] \mathbf{M}_{(1)}^k \mathbb{E} \left[ \mathbf{M}_{\neq 1}^k \right] + \mathbb{E}[\tau_h^k] \mathbf{P}_1 \mathbf{T}_{1(1)}^k \mathbb{E} \left[ \mathbf{H}_{\neq 1}^k \right]. \end{aligned} \quad (23)$$

The point estimates of the latent factor tensor  $\mathcal{T}_1^k$  can be obtained by solving the above Sylvester equation. The most intricate terms in this equation are  $\mathbf{H}_{\neq 1}^k$  and  $\mathbf{M}_{\neq 1}^k$ , and we explain them as follows. With  $\hat{\mathcal{H}}^k = \text{FCTN}(\mathcal{T}_1^k \times_1 \mathbf{P}_1, \mathcal{T}_2^k \times_2 \mathbf{P}_2, \mathcal{T}_3^k, \mathcal{T}_4^k)$  and using Eq. (3), we obtain the intricate term  $\mathbf{H}_{\neq 1}^k$  in the following equation  $\hat{\mathbf{H}}_{(1)}^k = \mathbf{T}_{1(1)}^k \mathbf{H}_{\neq 1}^k$ . Similarly, let  $\hat{\mathcal{M}}^k = \text{FCTN}(\mathcal{T}_1^k, \mathcal{T}_2^k, \mathcal{T}_3^k \times_3 \mathbf{P}_3, \mathcal{T}_4^k)$  and using Eq. (3), we obtain the  $\mathbf{M}_{\neq 1}^k$  in  $\hat{\mathbf{M}}_{(1)}^k = \mathbf{T}_{1(1)}^k \mathbf{M}_{\neq 1}^k$ . With the above approach, the factor tensor  $\mathcal{T}_1^k$  can be factored into independent variables, yielding its point estimate. The other factor tensors are estimated in a similar manner by constructing and solving their corresponding Sylvester equations detailed in the Appendix. A.

2) *Estimation of Hyperprior*: As shown in Fig. 2, the parameters  $\{\lambda_{n_1, n_2}^k\}$  establishes the connection between each factor tensor to form a full connected tensor network. The  $\lambda_{n_1, n_2}^k$  receives messages from its hyperprior and associated factor tensors, including  $\mathcal{T}_{n_1}^k$ , and  $\mathcal{T}_{n_2}^k$ . By applying Eq. (20), it has been shown that the posterior distribution of  $\lambda_{n_1, n_2}^k$  can be factorized as independent Gamma distributions (see Appendix. B for more details), as

$$q(\lambda_{n_1, n_2}^k) = \prod_r^{R_{n_1, n_2}} \text{Ga}((\lambda_{n_1, n_2}^k)_r | a_{n_1, n_2}^k, b_{n_1, n_2}^k), \quad (24)$$

with posterior parameters updated by

$$\begin{aligned} a_{n_1, n_2}^k &= a_0 + \frac{I_{n_1} \prod_{n \neq n_1, n_2}^N R_{n, n_1} + I_{n_2} \prod_{n \neq n_1, n_2}^N R_{n, n_2}}{2} \\ b_{n_1, n_2}^k &= b_0 + \frac{1}{2} \left( \mathbb{E}_q \left[ \mathbf{T}_{n_1(n_2)}^k(r) \mathbf{\Lambda}_{n_1, \neq n_2}^k \mathbf{T}_{n_1(n_2)}^k(r) \right] \right. \\ & \left. + \mathbb{E}_q \left[ \mathbf{T}_{n_2(n_1)}^k(r) \mathbf{\Lambda}_{n_2, \neq n_1}^k \mathbf{T}_{n_2(n_1)}^k(r) \right] \right), \end{aligned} \quad (25)$$

<sup>2</sup> $\mathbf{AXB} + \mathbf{CXD} = \mathbf{E} \Rightarrow \mathbf{x} = (\mathbf{B} \otimes \mathbf{A} + \mathbf{D} \otimes \mathbf{C})^{-1} \mathbf{e}$ , where  $\mathbf{x}$  and  $\mathbf{e}$  represent vectorization of  $\mathbf{X}$  and  $\mathbf{E}$ , respectively [10], [17].

where  $\lambda_{n_1, \neq n_2}^k = \lambda_{n_1, N}^k \odot \cdots \odot \lambda_{n_1, n_2+1}^k \odot \lambda_{n_1, n_2-1}^k \odot \cdots \odot \lambda_{n_1, n_1+1}^k \odot \lambda_{n_1, n_1-1}^k \odot \cdots \odot \lambda_{1, n_1}^k$ . Additionally,  $\mathbf{T}_{n_1(n_2)}^k$  represents the matrix form of the factor tensor  $\mathcal{T}_{n_1}^k$  unfolded along the  $n_2$ -th model. According to the FCTN decomposition defined in Eq. (1), the size of first dimension of  $\mathbf{T}_{n_1(n_2)}^k$  is  $R_{n_1, n_2}$ . The parameter  $a_{n_1, n_2}^k$  depends on the dimensions and tensor ranks associated with the subscripts  $n_1$  and  $n_2$ , while  $b_{n_1, n_2}^k$  is strongly correlated with the values of  $\mathcal{T}_{n_1}^k$  and  $\mathcal{T}_{n_2}^k$ .

3) *Estimation of Noise Precision Parameters*: The inference of the noise precision  $\tau_h^k$  is performed by receiving messages from its hyperprior and the observed image patches  $\mathcal{H}^k$  and hyperparameter  $c_0$ . Applying Eq. (20), the posterior distribution of  $\tau_h^k$  follows a Gamma distribution (see Appendix. C for more details), given by

$$q(\tau_h^k) = \text{Ga}(\tau_h^k | c^k, d^k), \quad (26)$$

where the posterior parameters can be updated by

$$\begin{aligned} c^k &= c_0 + \frac{I_1' I_2' I_3 I_4}{2} \\ d^k &= d_0 + \\ & \frac{1}{2} \mathbb{E}_q \left[ \left\| (\mathcal{H}^k - \text{FCTN}(\mathcal{T}_1^k \times_1 \mathbf{P}_1, \mathcal{T}_2^k \times_2 \mathbf{P}_2, \mathcal{T}_3^k, \mathcal{T}_4^k)) \right\|_F^2 \right]. \end{aligned} \quad (27)$$

In the above, the posterior parameter of  $c^k$  is determined by the dimensions of  $\mathcal{H}^k$  and hyperparameter  $c_0$ . The term  $\left\| (\mathcal{H}^k - \text{FCTN}(\mathcal{T}_1^k \times_1 \mathbf{P}_1, \mathcal{T}_2^k \times_2 \mathbf{P}_2, \mathcal{T}_3^k, \mathcal{T}_4^k)) \right\|_F^2$  can be interpreted as the residual between the after-downsampling in the spatial dimension of the fused image patches and the observed  $\mathcal{H}^k$ .

Similarly, the posterior distribution of the noise precision  $\tau_m^k$  also follows a Gamma distribution (see Appendix. D for more details), as

$$q(\tau_m^k) = \text{Ga}(\tau_m^k | e^k, f^k), \quad (28)$$

with posterior parameters updated by

$$\begin{aligned} e^k &= e_0 + \frac{I_1 I_2 I_3' I_4}{2} \\ f^k &= f_0 + \\ & \frac{1}{2} \mathbb{E}_q \left[ \left\| (\mathcal{M}^k - \text{FCTN}(\mathcal{T}_1^k, \mathcal{T}_2^k, \mathcal{T}_3^k \times_3 \mathbf{P}_3, \mathcal{T}_4^k)) \right\|_F^2 \right]. \end{aligned} \quad (29)$$

From Eq. (29), it is clear that the parameter  $e^k$  is derived from the dimensional of the observed  $\mathcal{M}^k$  and remains constant, while  $f^k$  represents the residual between the fused and observed image patches. According to the properties of the Gamma distribution, smaller residuals in Eq. (27) and (29) lead to higher expectation values of the corresponding precision parameters, which also reflects better fusion performance.

4) *Lower Bound of Model Evidence*: The proposed variational inference framework maximizes the *ELBO* defined in Eq. (18), which serves as the theoretical objective for convergence. The *ELBO* expression in Eq. (30) consists of two components:

$$ELBO = \mathbb{E}_{q(\Xi^k)} [\ln p(\mathcal{H}^k, \mathcal{M}^k, \Xi^k)] + H(q(\Xi^k)), \quad (30)$$

where the first term is the expected joint log-likelihood and the second term represents the entropy of the variational

distribution. Under the exponential family assumptions and conjugate priors, a closed-form expression of the *ELBO* is derived in Eq. (31), where all terms are analytically tractable:

*ELBO*

$$\begin{aligned}
&= -\frac{c^k}{2d^k} \mathbb{E}_q \left[ \left\| \mathcal{H}^k - \text{FCTN}(\mathcal{T}_1^k \times_1 \mathbf{P}_1, \mathcal{T}_2^k \times_2 \mathbf{P}_2, \mathcal{T}_3^k, \mathcal{T}_4^k) \right\|_F^2 \right] \\
&\quad - \frac{e^k}{2f^k} \mathbb{E}_q \left[ \left\| \mathcal{M}^k - \text{FCTN}(\mathcal{T}_1^k, \mathcal{T}_2^k, \mathcal{T}_3^k \times_3 \mathbf{P}_3, \mathcal{T}_4^k) \right\|_F^2 \right] \\
&\quad - \frac{1}{2} \sum_{n=1}^4 \text{Tr} \left\{ \mathbb{E}_q[\mathbf{A}_{n_1}^k] \left( \mathbf{T}_{n(n)}^k \top \mathbf{T}_{n(n)}^k \right) \right\} \\
&\quad + \sum_{n_1=1}^3 \sum_{n_2=n_1+1}^4 \sum_r^{R_{n_1, n_2}} \left\{ \ln \Gamma(a_{n_1, n_2}^k) \right. \\
&\quad \left. + a_{n_1, n_2}^k \left( 1 - \ln b_{n_1, n_2}^k - \frac{b_0^k}{b_{n_1, n_2}^k} \right) \right\} \\
&\quad + \ln \Gamma(c^k) + c^k \left( 1 - \ln d^k - \frac{d_0^k}{d^k} \right) \\
&\quad + \ln \Gamma(e^k) + e^k \left( 1 - \ln f^k - \frac{f_0^k}{f^k} \right) + C.
\end{aligned} \tag{31}$$

The structure of Eq. (31) offers an intuitive interpretation. The first two terms characterize the expected reconstruction errors of  $\mathcal{H}^k$  and  $\mathcal{M}^k$ , reflecting the model's fidelity to the observations. The third term imposes regularization through the factor tensor priors. The remaining terms quantify the divergence between posteriors and hyperpriors, serving as a natural penalty to control model complexity. In practice, the balance among these terms reflects the trade-off between data fidelity and model regularity during optimization (see Appendix. E for more details).

5) *Model Implementation and Complexity Analysis:* The implementation of the proposed BFCTN model for HMF proceeds as follows. Firstly, the observed LR-HSI  $\mathcal{H}$  and HR-MSI  $\mathcal{M}$  are chunked into overlapping patches of matched sizes and divided into  $K$  groups based on their column-wise spatial locations, yielding  $\mathcal{H}^k$  and  $\mathcal{M}^k$  for each group. Secondly, for each group  $k$ , the model introduces four latent factor tensors  $\{\mathcal{T}_n^k\}_{n=1}^4$  to capture shared spectral and spatial structures. These latent factors are inferred through a Bayesian process involving the estimation of parameters  $\{\boldsymbol{\lambda}_{n_1, n_2}^k\}_{1 \leq n_1 < n_2 \leq 4}$  governing their distributions, as well as noise precision parameters  $\tau_h^k$  and  $\tau_m^k$  for modeling the observation noise in  $\mathcal{H}^k$  and  $\mathcal{M}^k$ , respectively. The fused HR-HSI patches  $\{\mathcal{Z}^k\}_{k=1}^K$  are then obtained via the FCTN combination mechanism, inheriting enhanced spatial details from  $\mathcal{M}^k$  and preserving spectral fidelity from  $\mathcal{H}^k$ . Finally, the full-resolution HR-HSI  $\mathcal{Z}$  is reconstructed by aggregating  $\{\mathcal{Z}^k\}$  through averaging overlapping regions to ensure spatial consistency and smooth transitions. The proposed model is summarized in Algorithm 1.

To assess computational feasibility, the time complexity is analyzed as follows. Assuming all factor ranks are equal, i.e.,  $R_{n_1, n_2} = R$  for all  $1 \leq n_1 < n_2 \leq N$ , and all mode dimensions satisfy

$I_1 = I_2 = \dots = I_N = I$ , the computational cost mainly arises from the combination and estimation of factor tensors. The combination in Eqs. (26) and (28) incurs  $\mathcal{O}\left(N \sum_{n=2}^{N-1} R^{n(N-n)+n-1} I^n + NR^{2(N-1)} I + NR^{3(N-1)}\right)$  complexity. The estimation via solving the Sylvester equation in Eq. (23) contributes  $\mathcal{O}\left(NR^{2(N-1)} + NR^{3(N-1)} + NI^3\right)$ , assuming standard matrix equation solvers. In the BFCTN framework with fixed tensor order  $N = 4$ , the overall complexity for processing  $K$  groups simplifies to  $\mathcal{O}(KI^3R^6 + KR^9)$ . This reflects the trade-off between reconstruction fidelity and computational cost inherent in BFCTN.

---

#### Algorithm 1 BFCTN for LR-HSI and HR-MSI Fusion

---

**Input:**  $\mathcal{H}, \mathcal{M}, \mathbf{P}_1, \mathbf{P}_2, \mathbf{P}_3, sf$ .

**Output:** High-resolution hyperspectral image  $\mathcal{Z}$ .

- 1: Chunk  $\mathcal{H}$  and  $\mathcal{M}$  and divide into  $K$  groups.
  - 2: Initialize hyperparameters  $a_0, b_0, c_0, d_0, e_0, f_0$ , and parameters  $\{\mathcal{T}_n^k\}_{n=1}^4, \{\boldsymbol{\lambda}_{n_1, n_2}^k\}, \tau_h^k, \tau_m^k$ .
  - 3: **for**  $k = 1, \dots, K$  **do**
  - 4:     **while** *Iterations* < *max-iterations* **do**
  - 5:         *1) Estimate covariance parameters* *\**
  - 6:         **for**  $n_1 = 1, \dots, 3$  **do**
  - 7:             **for**  $n_2 = n_1 + 1, \dots, 4$  **do**
  - 8:                 Compute  $\hat{a}_{n_1, n_2}^k$  and  $\hat{b}_{n_1, n_2}^k$  via Eq. (25);
  - 9:                 Update  $q(\boldsymbol{\lambda}_{n_1, n_2}^k)$  by Eq. (24);
  - 10:             **end for**
  - 11:         **end for**
  - 12:         *2) Estimate noise precision parameters* *\**
  - 13:         Compute  $\hat{c}^k$  and  $\hat{d}^k$  via Eq. (27);
  - 14:         Update the posterior  $q(\tau_h^k)$  by Eq. (26);
  - 15:         Compute  $\hat{e}^k$  and  $\hat{f}^k$  via Eq. (29);
  - 16:         Update the posterior  $q(\tau_m^k)$  by Eq. (28);
  - 17:         *3) Estimate latent factor tensors* *\**
  - 18:         **for**  $n = 1, \dots, 4$  **do**
  - 19:             Establish the Sylvester equation as Eq. (23);
  - 20:             Update the point estimation of  $\mathcal{T}_n^k$ ;
  - 21:         **end for**
  - 22:         **end while**
  - 23:         Construct  $\mathcal{Z}^k$  by FCTN  $(\mathcal{T}_1^k, \mathcal{T}_2^k, \mathcal{T}_3^k, \mathcal{T}_4^k)$ .
  - 24:     **end for**
  - 25: Combine  $\{\mathcal{Z}^k\}_{k=1}^K$  into  $\mathcal{Z}$ .
- 

## IV. EXPERIMENTS AND DISCUSSION

This section presents the results of extensive experiments and a comprehensive analysis conducted to evaluate the performance of the proposed method. Experiments on conventional methods are run using MATLAB 2023a on a PC equipped with a 1.4 GHz quad-core Intel Core i5 processor and 16 GB of 2133 MHz LPDDR3 memory, while experiments involving deep learning based methods are conducted on a system with an M3 MAX processor and 64 GB of unified RAM.

### A. Baseline and Quantitative Metrics

In the field of HMF tasks, the effectiveness of methods needs to be verified by systematic comparisons across

TABLE I: The fusion performance of different methods in different scenarios is compared on the CAVE dataset.

SNR=35dB	sf=4				sf=8				sf=16			
	PSNR↑	SSIM↑	ERGAS↓	SAM ↓	PSNR ↑	SSIM↑	ERGAS↓	SAM↓	PSNR↑	SSIM ↑	ERGAS↓	SAM↓
LTTR	40.5335	0.9732	2.3478	15.3737	40.4722	0.9705	1.2882	16.1115	39.8726	0.9692	0.7377	16.3582
LTMR	40.4721	0.9735	2.3373	14.4449	40.3315	0.9705	1.3025	15.0552	39.7673	0.9671	0.7360	15.6794
GTNN	40.1069	0.9693	2.4413	15.5963	40.2650	0.9714	1.3187	14.7387	39.7292	0.969	0.7475	14.8752
CNMF	43.6854	0.9790	1.7442	14.0494	43.0677	0.9777	0.9667	13.1736	41.7560	0.9764	0.5472	13.7319
Hysure	44.4228	0.9796	1.5854	13.6379	42.1455	0.9752	1.0637	15.2437	40.0435	0.9679	0.7116	19.0891
NLSTF	44.6407	0.9739	1.5569	15.8824	43.8243	0.9719	0.9022	16.4862	43.0225	0.9708	0.5102	16.7782
CSTF	45.1114	0.9819	1.5218	9.7218	43.9305	0.9779	0.9100	10.9041	43.2382	0.9763	0.4972	<b>11.7565</b>
CTDF	44.5731	0.9754	1.6875	15.4104	43.7258	0.9729	0.9664	16.0499	42.9958	0.9705	0.5471	16.5415
JSSO	44.4057	0.9766	1.6515	14.8097	43.1283	0.9738	0.9779	15.4955	42.0972	0.9709	0.5533	16.2205
BGS-GTF	44.0998	0.9718	1.8255	14.7524	43.9275	0.9751	1.0540	13.4348	42.9904	0.9744	0.5957	12.9118
FCTN	39.9238	0.9422	2.7515	17.9608	39.3014	0.9371	1.5504	20.7791	39.8519	0.9538	0.7199	20.6506
<b>BFCTN</b>	<b>45.5716</b>	<b>0.9839</b>	<b>1.5051</b>	<b>9.1925</b>	<b>44.7692</b>	<b>0.9813</b>	<b>0.8246</b>	<b>10.2234</b>	<b>43.4067</b>	<b>0.9768</b>	<b>0.4928</b>	<b>11.8071</b>

sf=4	SNR=30dB				SNR=20dB				SNR=10dB			
	PSNR↑	SSIM↑	ERGAS↓	SAM ↓	PSNR ↑	SSIM↑	ERGAS↓	SAM↓	PSNR↑	SSIM ↑	ERGAS↓	SAM↓
LTTR	39.1668	0.9452	2.6493	20.6347	33.1139	0.7280	5.0356	32.9726	24.1907	0.2999	13.9589	43.2923
LTMR	39.3169	0.9491	2.5988	19.2410	33.8410	0.7522	4.6509	30.5259	25.2574	0.3222	12.4363	40.9665
GTNN	38.9318	0.9431	2.7207	19.8887	33.7008	0.7474	4.7345	30.6706	25.2776	0.3232	12.4152	41.1175
CNMF	42.2416	0.9620	2.0021	12.7530	35.3913	0.7920	3.8054	26.9579	25.5235	0.3677	12.2299	37.2262
Hysure	42.1788	0.9570	1.8998	18.5166	34.8497	0.7611	4.1139	29.9098	25.5975	0.3296	11.9135	40.4807
NLSTF	41.6080	0.9414	2.0341	21.7016	33.1815	0.7064	5.0047	33.7306	23.3800	0.2732	15.1707	43.9308
CSTF	43.7147	0.9720	1.7492	12.7808	36.0514	0.8219	3.8833	28.8187	23.4527	0.2410	16.4888	44.0105
CTDF	41.7851	0.9454	2.1364	20.8440	33.8516	0.7293	4.7601	31.8729	24.7087	0.3081	13.3563	42.1607
JSSO	41.7999	0.9493	2.0458	19.9852	34.4676	0.7594	4.2996	30.4015	26.4122	0.3950	10.6123	38.6408
BGS-GTF	41.3763	0.9402	1.6875	21.7235	32.9561	0.6855	5.5753	33.1500	23.0509	0.2283	17.2621	43.3803
FCTN	39.6824	0.9411	2.8033	18.5512	36.6623	0.8771	3.5900	24.4300	29.3674	<b>0.5427</b>	7.6629	35.8467
<b>BFCTN</b>	<b>44.2936</b>	<b>0.9767</b>	<b>1.6403</b>	<b>11.5959</b>	<b>38.9409</b>	<b>0.8976</b>	<b>2.6759</b>	<b>18.8010</b>	<b>30.1761</b>	<b>0.5421</b>	<b>7.0628</b>	<b>28.7665</b>

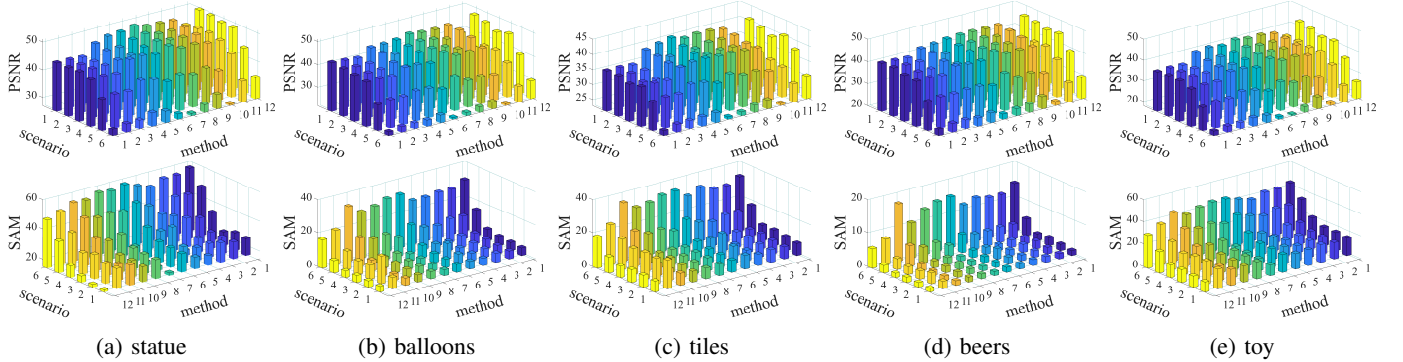


Fig. 3: The PSNR and SAM of the five images in CAVE dataset are compared by different methods in different scenarios. Method 1-12 correspond to LTTR, LTMR, GTNN, CNMF, Hysure, NLSTF, CSTF, CTDF, JSSO, BGS-GTF, FCTN, and BFCTN, respectively.

technology lines. The benchmark test set constructed in this study covers three types of mainstream paradigms: (1) the matrix decomposition methods are represented by CNMF [1] and Hysure [41]; (2) the tensor modeling system contains LTTR [6], LTMR [7], GTNN [40], NLSTF [4], CSTF [5], CTDF [19], JSSO [46], BGS-GTF [47], and FCTN [18], which together explore tensor a priori representations with different rank constraints; and (3) the deep learning system integrates emerging methods such as ZSL [42], M2U-Net [43], EDIP-Net [44], LRTN [45], reflecting the paradigm evolution from convolutional architectures to attention mechanisms.

To establish an evaluation system simultaneously assessing spectral-spatial fidelity, we select four metrics: Peak Signal-to-Noise Ratio (PSNR) [7], Structural Similarity (SSIM) [53], Error Relative Globale Adimensionnelle Synthèse (ER-

GAS) [52], and Spectral Angle Mapper (SAM) [1], forming a multiscale framework from local to global levels.

### B. Datasets Description

In this section, we introduce the three evaluation datasets and provide a detailed account of the process for generating synthetic LR-HSI and HR-MSI.

**CAVE Dataset<sup>3</sup>:** This dataset is acquired by an Apogee Alta U260 camera and consists of 32 indoor scenes captured by a composite pixel camera. Each image has dimensions of  $512 \times 512 \times 31$  pixels, where  $512 \times 512$  represents the spatial dimensions and 31 denotes the spectral bands, with wavelengths ranging from 400 nm to 700 nm at 10 nm intervals. The dataset encompasses a heterogeneous assortment

<sup>3</sup><https://www.cs.columbia.edu/CAVE/databases/multispectral/>

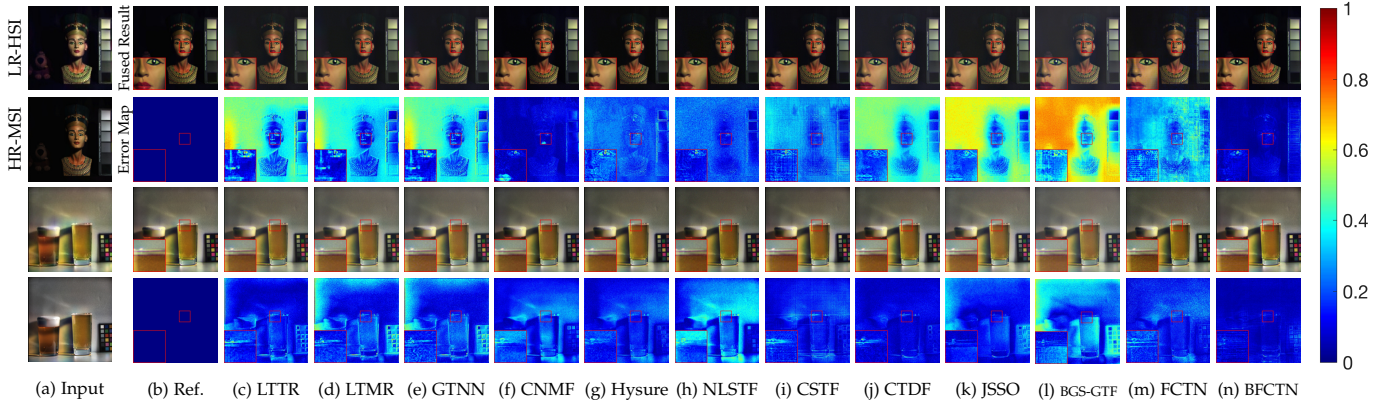


Fig. 4: Fusion results of other methods and BFCTN in Scenario1 on the 'statue' and 'beers' images in the CAVE dataset.

of natural and artificial materials, objects, shapes, and colors. Five representative images—including statue, balloons, tiles, beers, and toy—are selected to evaluate all approaches.

**Harvard Dataset<sup>4</sup>:** The dataset, provided by Harvard University, consists of 50 indoor and outdoor scenes captured under daylight illumination. Each image has dimensions of  $1040 \times 1392 \times 31$ , with spectral wavelengths spanning from 420 nm to 720 nm at 10 nm intervals. To facilitate a more accurate evaluation of all approaches, each image is cropped from the upper left corner to the size of  $512 \times 512 \times 31$ . Five representative images, including indoor and outdoor scenes—building (imga1), fruit (imgf8), car (imgc4), placard (imgd7), and wall (imge6)—are selected for evaluation.

**Pavia University Dataset<sup>5</sup>:** This dataset is acquired using the Reflective Optics System Imaging Spectrometer in Pavia, Italy, in 2003. The original dataset contains  $610 \times 340 \times 115$  pixels, with wavelengths spanning from 430 nm to 860 nm. After excluding bands affected by water vapor interference and those with low signal-to-noise ratios, a subset of  $256 \times 256 \times 91$  pixels is selected as the reference image.

The reference images are processed using the following approach to generate LR-HSI and HR-MSI. To generate LR-HSI, an averaging filter kernel of size  $sf \times sf$  is initially applied to the reference images, followed by downsampling by a factor of  $sf$ . HR-MSI is generated by downsampling the hyperspectral dimensions based on the spectral response function specific to each image. The spectral response function is obtained from a Nikon D700 camera for both the CAVE and Harvard datasets. The 31 bands of the reference images are reduced to 3 bands, resulting in HR-MSI images that are analogous to traditional RGB images. In the Pavia dataset, IKONOS-like reflective spectral response filters are applied to simulate HR-MSI with dimensions of  $256 \times 256 \times 4$ . In order to create a realistic simulation, Gaussian noise at a specified level is added to the generated LR-HSI and HR-MSI.

Although the Wald protocol [35] seeks to guarantee impartiality in comparative testing, previous studies still suffer from inconsistent inputs, unclear parameters, and opaque experimental scenarios, etc. To address these issues, we extended

the fairness protocol for comparing fusion methods, including but not limited to the following aspects:

- 1) To ensure the uniformity of all comparison experiments, all input images are generated using a consistent method.
- 2) All parameters of the comparison method are derived from the optimal settings described in the original paper without any additional optimisation or modification.
- 3) Comparison experiments are to be conducted under different downsampling factors and noise intensities with clearly defined experimental scenarios.

### C. Model Performance Evaluation

1) *Experimental Setup:* For our method, the hyperparameters  $a_0, b_0, c_0, d_0, e_0, f_0$  are empirically set to a small value of  $1 \times 10^{-6}$ . This choice serves as a non-informative prior and helps stabilize the inference process by avoiding the introduction of strong bias from the prior distribution. With the above, the initial values of  $\tau_h$  and  $\tau_m$  are to 1, and the parameters  $\lambda_{n_1, n_2}^k$  are initialized as all-one vectors. The initial factor tensors are randomly generated.

For data preprocessing, the input HR-MSI is chunked into small patches of  $64 \times 64$  pixels with an overlap of 48 pixels, while the corresponding LR-HSI is partitioned into patches of  $64/sf \times 64/sf$ , where  $sf$  denotes the spatial downsampling factor. The maximum number of iterations is set to six throughout all experiments. The ranks of the BFCTN are set to the following values for the purposes of the fusion test: [35, 4, 12, 4, 12, 4]. The experiments encompass a range of scenarios, including different downsampling factor ( $sf$ ) and  $SNR$  levels, for a total of six scenarios: Scenario 1:  $SNR=35\text{dB}$ ,  $sf=4$ ; Scenario 2:  $SNR=35\text{dB}$ ,  $sf=8$ ; Scenario 3:  $SNR=35\text{dB}$ ,  $sf=16$ ; Scenario 4:  $SNR=30\text{dB}$ ,  $sf=4$ ; Scenario 5:  $SNR=20\text{dB}$ ,  $sf=4$ ; Scenario 6:  $SNR=10\text{dB}$ ,  $sf=4$ .

2) *Experimental on CAVE Dataset:* A comprehensive experimental investigation is conducted on five experimental images of the CAVE dataset, encompassing six scenarios in the experimental setting. The objective is to evaluate and compare the performance of eleven traditional comparison methods alongside the proposed BFCTN. The numerical evaluation results presented in Tab. I are obtained by averaging the indicators of the five images, facilitating an intuitive

<sup>4</sup><http://vision.seas.harvard.edu/hyperspec/download.html>

<sup>5</sup><https://www.chu.edu/ccwintco/index.php/>

TABLE II: The fusion performance of different methods in different scenarios is compared on the Harvard dataset.

$SNR=35dB$	$sf=4$				$sf=8$				$sf=16$			
	PSNR $\uparrow$	SSIM $\uparrow$	ERGAS $\downarrow$	SAM $\downarrow$	PSNR $\uparrow$	SSIM $\uparrow$	ERGAS $\downarrow$	SAM $\downarrow$	PSNR $\uparrow$	SSIM $\uparrow$	ERGAS $\downarrow$	SAM $\downarrow$
LTTR	41.9097	0.9733	2.6712	2.7895	42.2786	0.9745	1.6403	3.1136	42.4026	0.9747	0.9428	3.4836
LTMR	42.2513	0.9745	2.2957	2.7700	42.7363	0.9762	1.2254	3.1096	42.6472	0.9755	0.7095	3.5532
GTNN	41.9536	0.9711	2.3711	3.0533	42.6466	0.9758	1.2372	3.1343	42.7943	0.9764	0.6941	3.4566
CNMF	45.2396	0.9825	1.8666	2.4334	44.7029	0.9822	0.9764	2.5801	43.9750	0.9804	0.5108	2.6473
Hysure	45.5182	0.9818	2.1539	2.5345	44.4464	0.9806	1.1151	2.9570	44.2252	0.9806	0.5678	3.1677
NLSTF	45.2475	0.9798	2.2268	2.6322	44.9025	0.9795	1.1328	2.7315	44.6631	0.9796	0.5747	2.7910
CSTF	45.5062	0.9808	1.8356	2.4953	45.2793	0.9805	<b>0.9357</b>	2.5765	45.0993	0.9804	<b>0.4775</b>	<b>2.6410</b>
CTDF	45.2974	0.9782	2.0382	2.7195	44.9059	0.9776	1.0620	2.8350	44.5474	0.9769	0.5722	2.9624
JSSO	45.2707	0.9789	2.0817	3.2855	44.6178	0.9778	1.0724	2.8340	44.6178	0.9774	0.5480	2.9122
BGS-GTF	45.3475	0.9795	1.9316	2.6939	44.8203	0.9788	0.9856	2.7144	44.8203	0.9786	0.5091	2.8153
FCTN	42.8358	0.9691	2.3183	2.6440	43.7690	0.9749	1.1072	3.2457	41.1380	0.9540	1.0456	4.7776
<b>BFCTN</b>	<b>45.8808</b>	<b>0.9830</b>	<b>1.8353</b>	<b>2.3847</b>	<b>45.6024</b>	<b>0.9826</b>	0.9406	<b>2.4976</b>	<b>45.1332</b>	<b>0.9815</b>	0.5071	2.6425

$sf=4$	$SNR=30dB$				$SNR=20dB$				$SNR=10dB$			
	PSNR $\uparrow$	SSIM $\uparrow$	ERGAS $\downarrow$	SAM $\downarrow$	PSNR $\uparrow$	SSIM $\uparrow$	ERGAS $\downarrow$	SAM $\downarrow$	PSNR $\uparrow$	SSIM $\uparrow$	ERGAS $\downarrow$	SAM $\downarrow$
LTTR	40.5957	0.9607	3.3441	3.4718	34.7317	0.8284	7.5154	8.0674	26.0003	0.4336	20.6733	20.4302
LTMR	41.1664	0.9639	2.6832	3.3308	35.7396	0.8502	5.7702	7.1228	26.9195	0.4609	18.0715	18.5992
GTNN	40.8697	0.9598	2.7591	3.6596	35.5256	0.8434	5.9111	7.4447	26.9308	0.4616	18.0808	18.7175
CNMF	44.1168	0.9759	2.0595	2.8119	37.3961	0.8816	4.0419	6.4516	27.4888	0.5073	12.5086	17.8248
Hysure	44.5412	0.9762	2.3096	2.7975	38.9690	0.9035	3.4328	5.0485	28.5060	0.5170	13.4146	16.0014
NLSTF	42.9151	0.9651	3.0635	3.4363	35.1294	0.8225	7.5372	8.3557	25.4193	0.4080	22.6059	21.6852
CSTF	45.1177	0.9787	1.8830	2.5851	38.8764	0.9078	3.7190	5.4473	25.4159	0.3770	22.7173	22.6101
CTDF	43.1215	0.9632	2.6949	3.5153	35.5798	0.8283	6.7639	8.1149	26.2244	0.4355	18.0391	20.7401
JSSO	43.3163	0.9659	2.6504	3.4057	36.9816	0.8747	5.5484	6.6828	28.9617	0.5796	13.3913	15.0167
BGS-GTF	43.9173	0.9715	2.2391	3.1782	36.1647	0.8482	5.9833	7.8325	25.1843	0.3750	22.7556	23.5266
FCTN	42.6357	0.9672	2.3450	3.2866	40.6183	0.9413	2.7292	3.9614	33.0894	0.7254	<b>6.0059</b>	8.9635
<b>BFCTN</b>	<b>45.4224</b>	<b>0.9808</b>	<b>1.8791</b>	<b>2.4667</b>	<b>41.8917</b>	<b>0.9517</b>	<b>2.3993</b>	<b>3.2292</b>	<b>33.2077</b>	<b>0.7379</b>	6.4861	<b>8.1082</b>

assessment of the performance of the various methods on the CAVE dataset. As evidenced in Tab. I, the BFCTN exhibits superior performance compared to other comparison methods across all resolutions, particularly in the context of Scenario 2, where its indicators significantly surpass those of all comparison methods. Furthermore, methods such as CNMF, CSTF, and Hysure demonstrate high performance under high  $SNR$  conditions, whereas methods such as LTTR and LTMR exhibit relatively poor performance. As the  $SNR$  decreases to 30 dB, 20 dB, and 10 dB, the BFCTN continues to demonstrate superior performance across all indicators. Furthermore, CSTF and FCTN demonstrate robustness under medium  $SNR$  conditions, whereas the performance of other comparison methods, except BFCTN, declines considerably at lower  $SNR$  levels. Fig. 3 provides a visual representation of the comprehensive fusion performance of different methods for each image under all input scenarios, clearly showing that BFCTN exhibits excellent fusion performance across various images and all  $SNR$  and downsampling factor conditions.

Fig. 4 presents the output and error maps for two images with contrasting backgrounds in Scenario 1: a darker image of a 'statue' and a brighter image of 'beers'. The initial row of each set of images presents a false color composite image synthesized by bands 28, 16, and 1, while the subsequent row illustrates the error image between the fusion result and the reference image. Fig. 4 (a) depicts the LR-HSR and HR-MSI used for fusion. Fig. 4 (b) shows the reference image, and Figs. 4 (c)-(n) show the fusion results of the eleven comparison methods and proposed BFCTN.

Overall, all experimental methods effectively extract high-resolution details from the HR-MSI and fuse them with the LR-HSI to generate satisfactory HR-HSI. However, from the

locally magnified details and error images, in the 'statue' image with a darker background, the LTTR, LTMR, GTNN, CTDF, JSSO and BGS-GTF exhibit significant discrepancies from the reference image in the error maps. The CNMF performs well overall in fusion but has noticeable errors in the locally magnified portrait area. The Hysure and NLSTF introduce a significant amount of noise after fusion, while the CSTF and FCTN cause severe distortion in the darker background areas. For the 'beers' image with a brighter background, the fusion effect of the various methods improves in the background. However, the LTMR, GTNN, and NLSTF still show distortions at the background edges. Additionally, the LTTR, CNMF, CSTF, CTDF and BGS-GTF show pronounced streaks and artifacts around the cup edge in the magnified area, while the FCTN still exhibits a considerable degree of noise. In contrast, BFCTN demonstrates superior clarity in the false-color images, with sharper edges and smoother error maps.

3) *Experimental on Harvard Dataset:* In addition, we also conduct comparative experiments in six scenarios on five images of the Harvard dataset. Tab. II illustrates the assessment outcomes on the Harvard dataset, wherein the proposed BFCTN exhibits optimal performance across a range of metrics in diverse scenarios. It is worthy of note that in Scenarios 2, 3 and 6, the optimal ERGAS values are achieved by CSTF and FCTN, respectively. This phenomenon can be attributed to the potential for significant errors in specific bands or local areas of the fused image. Furthermore, it is notable that under conditions of high noise, the performance of FCTN markedly surpasses that of other comparison methods, approaching the performance of the proposed BFCTN.

To facilitate a more intuitive comparison of the performance of comparison methods alongside the proposed BFCTN under

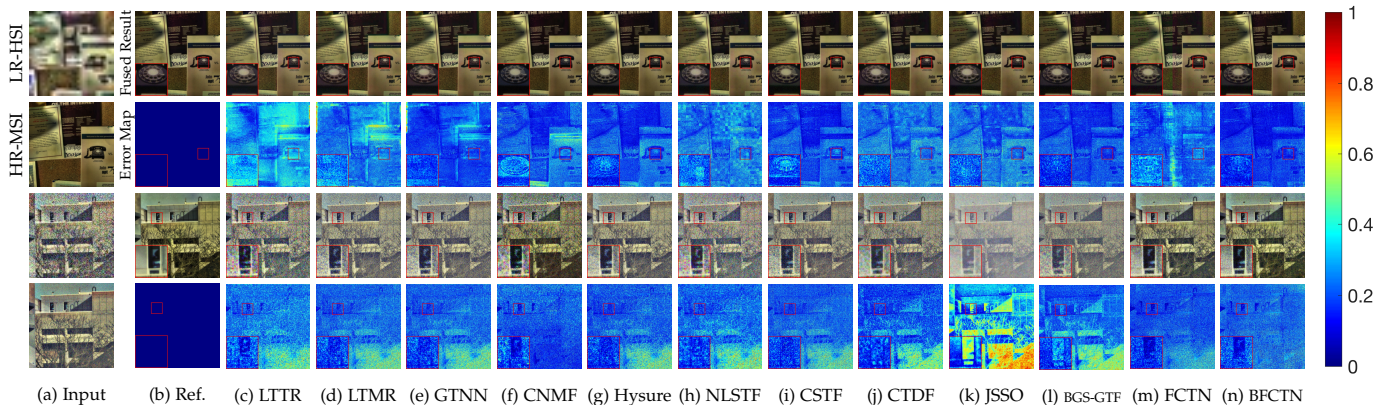


Fig. 5: Fusion results of other methods and proposed BFCTN on the 'placard' and 'building' images in the Harvard dataset. The 'placard' image is experimented with in Scenario 3, while building is experimented with in Scenario 6.

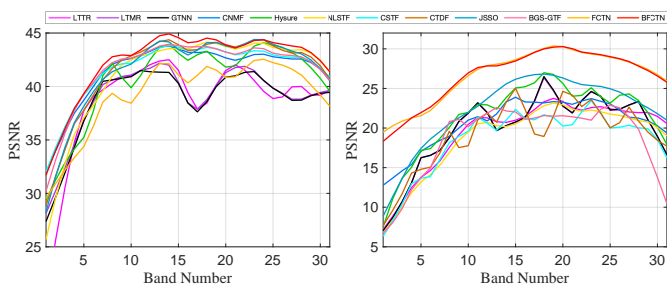


Fig. 6: The PSNR of each fusion result of 'placard' and 'building' along the spectral bands

two low-quality input scenarios, we select one indoor image 'placard' and one outdoor image 'building' for display in Fig. 5. The 'placard' is experimented with in Scenario 3, while the 'building' is experimented with in Scenario 6. As can be observed in Fig. 5 (a), strong blur and high noise are clearly evident in the 'placard' and 'building', respectively. Unlike the CAVE dataset, false-color images for the Harvard dataset are synthesized using bands 20, 15, and 8. Upon examination of the fusion results for the 'placard', it becomes evident that even with sparser sampling, satisfactory outcomes can still be achieved. However, it is notable that there are discernible differences in the details observed among the methods. The LTRR, LTM, CTDF and JSSO exhibit significant color distortion, and the GTNN shows numerous streaks in the error map. The fusion images from CNMF, Hysure, and NLSTF retain a significant amount of noise. In contrast, the CSTF and FCTN produce images with high clarity, but they also exhibit significant errors in darker background areas. In the case of the 'building' image, higher noise levels are applied, resulting in the majority of methods retaining a considerable amount of noise in their fusion results. Only the CNMF, FCTN, and BFCTN demonstrate satisfactory performance. However, in the locally magnified areas of the false-color image, the first two exhibit severe blurring, while the BFCTN maintains clear details and sharp edges.

Furthermore, the distinct bands are subjected to visual analysis with regard to the two aforementioned images, as

illustrated in Fig. 6. In the highly blurred 'placard' image, the proposed BFCTN achieves favorable results, with smooth lines (red) maintaining the highest PSNR in most locations. In the 'building' image affected by strong noise interference, both the FCTN and BFCTN significantly outperform other methods. The advantage of BFCTN over FCTN is relatively minor, indicating that the FCTN also exhibits robust performance.

#### D. Deep Learning Baseline Comparison

The aforementioned analysis proved the effectiveness of BFCTN against conventional methods. However, recent advances in the field of deep learning have introduced the latest paradigm of hyperspectral multispectral image fusion. In order to comprehensively position our proposed method in the contemporary research field, we extend our comparative analysis to four representative state-of-the-art deep learning methods: ZSL [42], M2U-Net [43], EDIP-Net [44], and LRTN [45]. These methods are selected for their established spectral-spatial reconstruction performance and open-source implementations. Specifically, we respectively selected the

TABLE III: Comparison results with advanced deep learning methods.

$SNR$	Dataset	Method	PSNR $\uparrow$	SSIM $\uparrow$	ERGAS $\downarrow$	SAM $\downarrow$
30dB	CAVE	ZSL	34.2167	0.9063	1.5111	19.6241
		M2U-Net	39.4336	0.9419	1.0719	12.6855
		EDIP-Net	<u>39.7096</u>	<u>0.9445</u>	<u>0.9868</u>	<b>12.5048</b>
		LRTN	38.7608	0.9404	1.0911	15.7430
		BFCTN	<b>39.8753</b>	<b>0.9517</b>	<b>0.9711</b>	14.9580
	Harvard	ZSL	40.6948	0.9577	8.4937	7.8108
		M2U-Net	46.1575	0.9823	<u>2.2935</u>	<u>4.4542</u>
		EDIP-Net	47.3979	<u>0.9854</u>	2.4114	4.8031
		LRTN	41.6276	0.9721	3.1580	7.5513
		BFCTN	<b>47.9209</b>	<b>0.9877</b>	<b>1.8129</b>	<b>4.2952</b>
10dB	CAVE	ZSL	20.0787	0.2096	8.4254	43.0520
		M2U-Net	29.7534	0.8388	2.6536	23.4079
		EDIP-Net	<u>30.0779</u>	<b>0.8413</b>	<u>2.5507</u>	<u>23.6223</u>
		LRTN	22.4170	0.3264	6.2037	38.1593
		BFCTN	<b>30.4776</b>	<b>0.7299</b>	<b>2.4536</b>	<b>23.0515</b>
	Harvard	ZSL	27.2621	0.5439	17.2224	29.6534
		M2U-Net	34.9699	<u>0.8825</u>	5.4545	10.0532
		EDIP-Net	35.0370	0.8814	5.4160	10.0521
		LRTN	27.9139	0.5125	22.5027	34.4219
		BFCTN	<b>41.2420</b>	<b>0.9450</b>	<b>3.3745</b>	<b>7.2982</b>

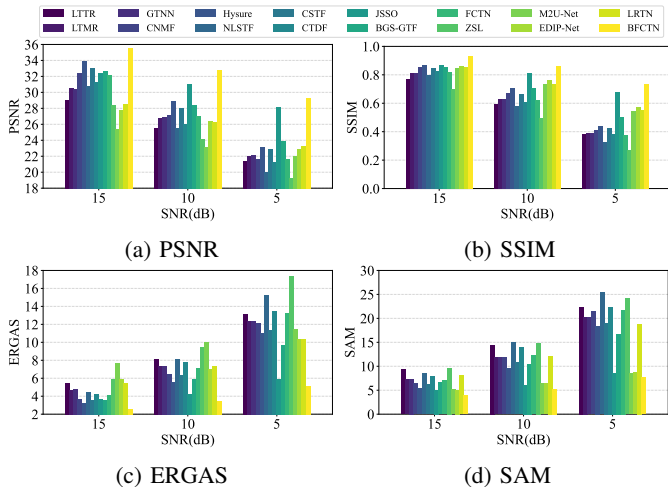


Fig. 7: Properties of different methods for Pavia University datasets under high noise conditions.

CAVE ('toy') and Harvard ('imgf8') datasets. Building on previous observations that fusion results exhibit low sensitivity to the downsampling factor ( $sf$ ), we fix  $sf = 8$  in this section to focus on evaluating performance under varying additive noise levels, consistent with established protocols.

Tab. III shows the quantitative results, under low noise scenario (30dB), BFCTN achieves the highest PSNR, SSIM, and ERGAS scores on the CAVE dataset, though it slightly underperforms in SAM compared to ZSL and M2U-Net. On the Harvard dataset, BFCTN consistently outperforms all four deep learning baselines across all metrics, highlighting its robustness in more complex scenarios. In high-noise scenario (10dB), BFCTN maintains leading performance in PSNR, ERGAS, and SAM for the CAVE dataset, while exhibiting a marginal deficit in SSIM against EDIP-Net and LRTN. Notably, it secures comprehensive superiority on the Harvard dataset, even under severe noise degradation. These results suggest that while deep learning methods excel in certain spectral or structural metrics (e.g., SAM or SSIM), BFCTN provides more reliable and generalizable reconstruction quality, particularly in challenging noise environments. The unsatisfactory performance of ZSL and LRTN under high-noise conditions mainly arises from their sensitivity to distributional shifts. Although ZSL aims to generalize without retraining, its reconstruction heavily depends on feature similarity learned from clean training distributions, leading to degraded estimation when the spectral observations are heavily corrupted. Likewise, the deterministic low-rank constraint in

LRTN lacks explicit noise modeling, making it less robust to severe perturbations.

### E. Model Robustness Evaluation

In previous experiments, the proposed BFCTN consistently delivers exceptional performance across a wide range of scenarios. It is noteworthy that both BFCTN and FCTN demonstrate superior performance compared to other methods in low  $SNR$  scenarios. To further evaluate the noise immunity of FCTN in comparison to the proposed BFCTN and test the robustness of various methods, comparative experiments are conducted with special emphasis on extremely low  $SNR$  scenarios. Given that the dimensions of the Pavia University dataset following cropping are  $256 \times 256$ , the ranks of BFCTN are adjusted to [35, 4, 3, 4, 3, 2] to align with these dimensions. The parameters of other compared methods are set in accordance with the original paper's specifications. For some methods lacking explicit Pavia University dataset parameters, the previous parameters are utilized in the experiments.

Fig. 7 illustrates the performance of eleven comparison methods and the proposed BFCTN on the Pavia University  $SNR$  levels of 15, 10, and 5 dB, as presented in bar charts. The yellow bars represent the proposed BFCTN, which is observed to outperform other methods in numerical terms. Moreover, FCTN, which is also based on FCTN decomposition, exhibits robust performance under conditions of extremely low  $SNR$ .

Fig. 8 illustrates the fused images obtained using various methods at an  $SNR$  of 5 dB. The initial row presents false-color images synthesized from bands 42, 15, and 8. Although CNMF is effective in reducing noise, it introduces the most conspicuous color distortion. In contrast to the other methods, BFCTN not only eliminates noise but also preserves image details with exceptional accuracy. In the magnified regions, only FCTN, M2U-Net, EDIP-Net and BFCTN effectively restore the shrub details. However, the FCTN produces images with blurring and artifacts in other areas, and some noise from M2U-Net and EDIP-Net still remains. The second row displays the error images of the fused results in comparison to the ground truth. It is evident that BFCTN produces darker and smoother error images. In the presence of significant noise interference, the fusion performance of BFCTN is demonstrably superior to that of other methods.

### F. Evaluation on Real Dataset

To validate the practical applicability of the proposed method, we conducted experiments on a real-world dataset

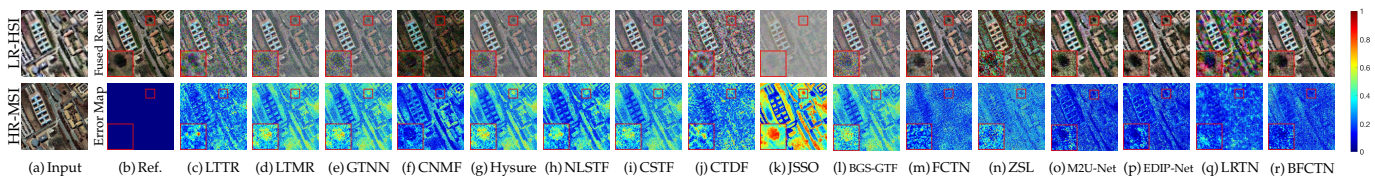


Fig. 8: Fusion results of other methods and BFCTN on the Pavia University dataset. Input images are subjected to Gaussian white noise with  $SNR = 5$ dB, and the LR-HSI is downsampled by a factor of  $sf = 4$ .

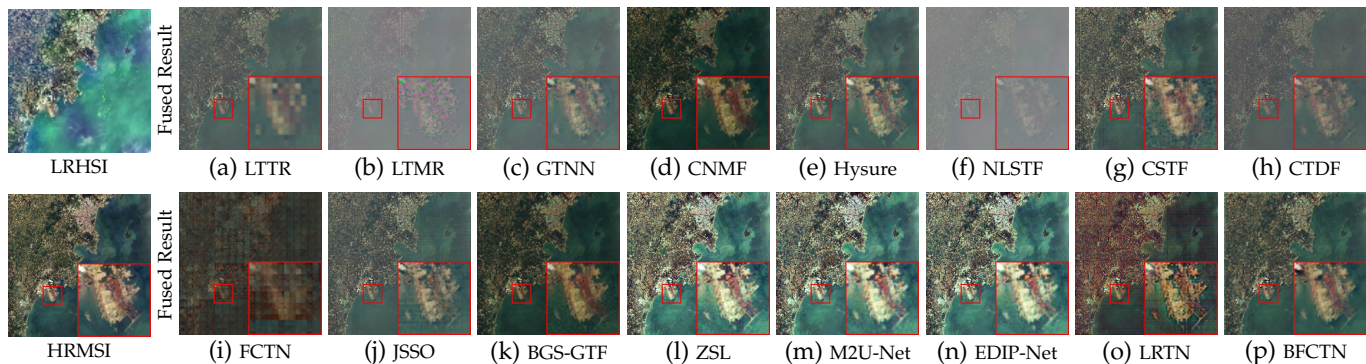


Fig. 9: Fusion results of all comparison methods and BFCTN on real datasets.

TABLE IV: Comparison of quantitative indices (NHQM $\downarrow$ ) of different methods on the real data.

LTTR	LTMR	GTNN	CNMF	Hysure	NLSTF	CSTF	CTDF	FCTN	JSSO	BGS-GTF	ZSL	M2U-Net	EDIP-Net	LRTN	BFCTN
28.76	26.96	27.27	26.05	25.53	27.08	24.69	28.67	29.55	25.52	27.43	26.54	26.42	26.54	27.57	24.44

acquired by the Ziyuan(ZY)-02D satellite. The dataset contains spatially co-registered LR-HSI, HR-MSI, and panchromatic (PAN) data. The original LR-HSI has dimensions of  $6213 \times 6099 \times 166$  with spectral coverage from 395 to 2501 nm, while the HR-MSI measures  $2071 \times 2033 \times 8$  bands. We removed long-wavelength bands with relatively low signal-to-noise ratios and selected 76 spectral bands covering visible and near-infrared regions. A  $800 \times 800 \times 76$  subregion is cropped and downsampled as the LR-HSI, with a corresponding  $100 \times 100 \times 8$  subregion extracted from the HR-MSI. Based on the CNMF degradation modeling framework, we improved the estimation process of the spectral response function (SRF). Specifically, on the basis of nonnegative constraints, a normalization constraint (ensuring that the sum of response coefficients in each channel equals one) and a spectral smoothness regularization term were introduced to avoid unreasonable oscillations between adjacent bands. At the same time, a weighting mechanism was applied to enhance robustness to invalid pixels. Using the updated SRF, the point spread function (PSF) was further estimated to enhance the stability of spatial degradation modeling, making the obtained degradation kernels more consistent with the physical characteristics of the imaging system and providing reliable priors for subsequent fusion.

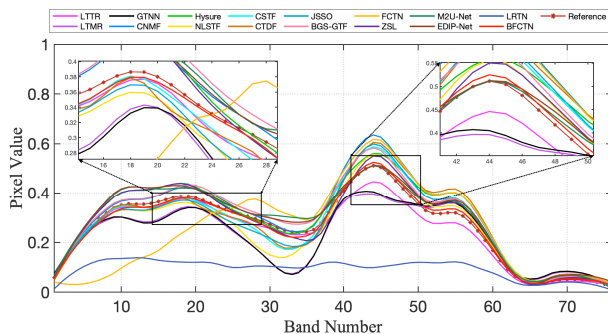


Fig. 10: The spectral characteristic curves of all methods and input LR-HSI at [120,120] pixel positions.

In the absence of ground-truth references, the evaluation relied on the physical plausibility of the spatial texture and the consistency of the spectral features with the input LR-HSI. Visually, as shown in Fig. 9, BFCTN achieves an optimal balance between spatial enhancement and spectral preservation, as evidenced by minimized artifacts, spatial clarity close to HR-MSI, and the absence of spectral aberrations in vegetated areas. Furthermore, Tab. IV reports the no-reference hyperspectral quality metric (NHQM) [60] results, where BFCTN achieves the highest score, further confirming its superior capability improve spatial details on real data. In addition, Fig. 10 demonstrates the comparison of the spectral features of the outputs of each method with the input LR-HSI at a random pixel, and the outputs of CSTF, EDIP-Net and BFCTN maintain a high degree of consistency with the spectral features of the input image. The above comparison shows that BFCTN has excellent ability to fuse real datasets.

### G. Time Overhead Analysis

Tab. V summarizes the time requirements for each method. Due to the training requirements of deep learning methods, this comparison is not made. The proposed BFCTN requires multiple high-order tensor decompositions, which is a more time-consuming process than methods based on matrix decomposition and sparse tensor decomposition. However, our method is significantly faster than FCTN, which is based on the same decomposition paradigm. This is because FCTN raises the data to the 5-th order, introducing greater computational overhead with increasing dimensions, slowing down the convergence of the model. Thus, BFCTN strikes an effective balance between time cost and fusion performance.

### H. Discussion

This section discusses BFCTN from the perspectives of architectural effectiveness and implementation, including the contribution of the Gamma prior, FCTN-ranks selection, chunking and overlapping strategies, the impact of various spatial degradation kernels, and the model convergence analysis.

TABLE V: Average running time(seconds) of different methods.

Datasets	LTR	LTMR	GTNN	CNMF	Hysure	NLSTF	CSTF	CTDF	JSSO	BGS-GTF	FCTN	BFCTN
CAVE	352.05	230.10	243.45	38.70	127.17	69.71	119.84	48.24	5.55	178.42	3251.52	849.98
Harvard	348.12	256.97	273.52	50.07	144.08	77.16	135.37	76.95	4.31	149.27	2963.19	922.94
Pavia University	78.65	154.82	75.41	7.89	22.32	26.04	85.99	11.08	1.87	106.81	890.27	89.01
Real Dataset	457.76	362.96	381.27	58.05	198.53	96.08	244.39	116.67	12.55	232.52	3499.43	1321.44

All experiments are conducted using the 'toy' image from the CAVE dataset as the test subject.

1) *Contribution of Hierarchical Sparsity Priors*: To verify the validity of the hierarchical sparsity prior, we compared the original model with Gamma distribution and the variant with fixed sparse constraints. The test group replaced the Gamma distributions of the top-level parameters  $\tau_h^k$ ,  $\tau_m^k$  and  $\lambda_{(n_1, n_2)}^k$  with constants ( $C \in \{1e-2, 1e-1, 1\}$ ), and left the rest of the model settings unchanged. The experiments are executed with three parameter configurations ( $\lambda$  fixed (include  $\lambda_{(n_1, n_2)}^k$ ),  $\tau$  fixed (include  $\tau_h^k$  and  $\tau_m^k$ ), and full parameter fixed) are tested, and the performance metrics on the dataset are recorded.

Tab. VI shows the quantitative results, where the  $\lambda$  shows good robustness (fluctuations of  $< 0.4$  dB in the range of 1e-2 to 1), while the  $\tau$  exhibits strong sensitivity (6.2 dB decrease in PSNR when fixed to 1e-2 and only 0.1 dB when fixed to 1). It is noteworthy that when both  $\lambda$  and  $\tau$  are fixed to constants, the results seem to possess the properties of the above two parameter configurations, with stable but lower results than the original configuration when fixed at smaller values, and performance closer to the original configuration when fixed at 1. These results not only verify the validity of the hierarchical Gamma prior mechanism, but also show its certain ability to be parameter free and provide more stable results.

2) *Effect of FCTN-ranks*: In Eq. (1), the FCTN-ranks consist of a set of numbers  $(R_{1,2}, \dots, R_{1,N}, \dots, R_{N-1,N})$ . In the proposed model, given that the tensor to be decomposed has the same scale in the first and second dimensions, it is reasonable to consider  $R_{1,3}$  and  $R_{2,3}$  to be equivalent, as well as  $R_{1,4}$  and  $R_{2,4}$ . Then the parameters of the rank are restricted to four, i.e., we use  $R1$  to denote  $R_{1,2}$ ,  $R2$  to denote  $R_{1,3}$  and  $R_{2,3}$ ,  $R3$  to denote  $R_{1,4}$  and  $R_{2,4}$ , and  $R4$  to denote  $R_{3,4}$ . Further, we categorize them into two groups and discuss the synergistic influence relationship between  $R1$ ,  $R4$  and  $R2$ ,  $R3$ , respectively. As Fig. 11 (a) illustrates, larger  $R1$  values result in better performance, while improvements with  $R4$  diminish beyond 4. Balancing time cost and performance, we select  $R1$  as 35 and  $R4$  as 4. Additionally, from Fig. 11(b), we observe a slight performance drop for  $R2$  beyond 4, while  $R3$  shows steady improvement. Thus, we set  $R2$  to 4 and  $R3$  to 12. The final FCTN-ranks are determined to be [35, 4, 12, 4, 12, 4].

3) *Effect of Chunking and Overlapping*: To optimize the chunking and overlapping strategies parameters, we designed controlled experiments. The system evaluates the combination of patch size  $m \in \{16, 32, 64, 128\}$  with overlapping region  $p$  (grouping constraint:  $\frac{W-p}{m-p} + 1 = K$ ). As shown in Fig. 12 (a), the optimal PSNR is obtained for  $m=64$  with  $p=48$  ( $3m/4$  overlap), which is a 1.0 dB improvement over the suboptimal combination ( $m=32$ ,  $p=16$ ). When  $m=512$  is set (i.e., the full group input is not chunked), the model degrades to a third-

TABLE VI: Comparison between Gamma prior and fixed parameters.

Configuration	PSNR $\uparrow$	SSIM $\uparrow$	ERGAS $\downarrow$	SAM $\downarrow$
Original (Gamma)	<b>42.7628</b>	<b>0.9764</b>	<b>1.4199</b>	<b>10.5293</b>
$\lambda$ fixed	1e-2	41.4363	0.9735	1.6196
	1e-1	41.4164	0.9735	1.6321
	1	41.8382	0.9761	1.5178
$\tau$ fixed	1e-2	36.5949	0.8920	2.5775
	1e-1	41.7180	0.9744	1.5010
	1	42.6246	0.9745	1.4578
$\lambda$ & $\tau$ fixed	1e-2	41.3683	0.9732	1.6250
	1e-1	41.3771	0.9733	1.6213
	1	42.2795	0.9728	1.5315

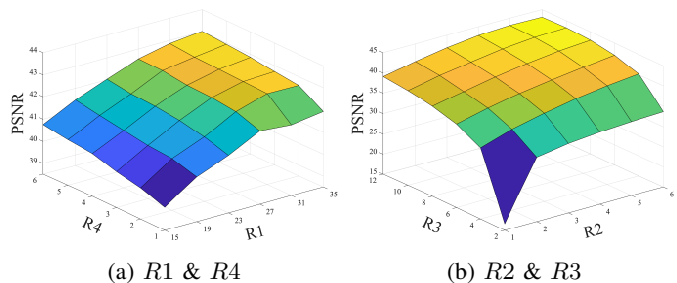


Fig. 11: The rank selection strategy in the proposed method.

order tensor network structure. The experimental data show that the model performance metrics drop significantly in this case, and this comparison result strongly validates the design effectiveness of the chunking strategy.

Fig. 12 (b) demonstrates the effect of different parameters on the time overhead, it is worth mentioning that the different combinations directly affect the  $K$ -value, the model is processed in groups, and the different group number  $K$  do not affect the model performance, but its effect on the time performance is larger. Combining performance and computational cost, the model selects a patch size of 64 and an overlap size of 48.

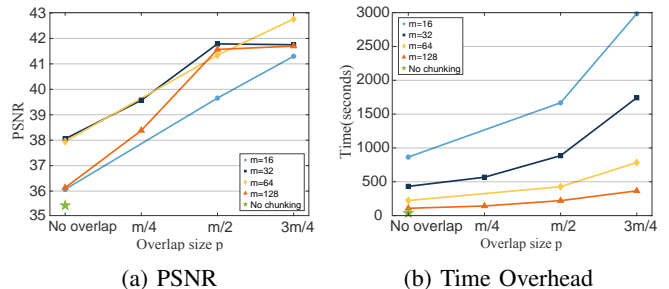


Fig. 12: Analysis of performance and time overhead by different chunking and overlapping strategies.

4) *Degradation Kernels Comparison*: To systematically investigate the impact of kernel separability assumptions on fusion performance, we design a controlled experiment with four representative degradation kernels, which include:

- **Average kernel**:  $4 \times 4$  average kernel.
- **Gaussian kernel**  $G_{4 \times 4}$ :  $\sigma = 2$  with  $4 \times 4$  support.
- **Gaussian kernel**  $G_{7 \times 7}$ :  $\sigma = 2$  with  $7 \times 7$  support.
- **Motion blur kernel**  $M_{30^\circ}$ : length = 4 and  $\theta = 30^\circ$ .
- **Motion blur kernel**  $M_{45^\circ}$ : length = 4 and  $\theta = 45^\circ$ .
- **Elliptical kernel**  $E_{30^\circ}$ : Anisotropic Gaussian blur with  $\sigma_x = 1$ ,  $\sigma_y = 3$ , and rotation angle  $\theta = 30^\circ$ , simulating non-isotropic optical defocus.
- **Hybrid kernel**  $H_{G+M}$ : Convolution of a Gaussian kernel ( $\sigma = 2$ ) and a motion blur kernel (length = 4,  $\theta = 30^\circ$ ), representing compound degradations combining defocus and motion effects.
- **Sensor-specific kernel**  $S_{\text{var}}$ : Channel-dependent Gaussian blurs with increasing  $\sigma$  across spectral bands, modeling heterogeneous spatial responses of multi-sensor imaging systems.

Where the average and Gaussian kernels can be exactly decomposed into the outer product of 1D vectors and are therefore regarded as separable kernels, the motion blur, elliptical, hybrid, and sensor-varying kernels are non-separable due to their directional or spatially heterogeneous characteristics. For methods that require the decomposition of the point spread function (PSF), such non-separable kernels are approximated by performing an SVD-based low-rank factorization after zero-padding.

TABLE VII: The performance of BFCTN under different degradation kernels.

Kernel	PSNR $\uparrow$	SSIM $\uparrow$	ERGAS $\downarrow$	SAM $\downarrow$
Average	42.7628	0.9764	1.4199	10.5293
$G_{4 \times 4}$	42.9082	0.9760	1.3915	10.4246
$G_{7 \times 7}$	42.2129	0.9743	1.4976	10.8569
$M_{30^\circ}$	41.4712	0.9723	1.5288	10.4926
$M_{45^\circ}$	41.3125	0.9718	1.5531	10.6378
$E_{30^\circ}$	40.9856	0.9702	1.6024	10.9845
$H_{G+M}$	41.2728	0.9765	1.5733	10.7319
$S_{\text{var}}$	40.8651	0.9669	1.7440	11.5923

TABLE VIII: The performance of various methods under the motion blur kernel.

Method	PSNR $\uparrow$	SSIM $\uparrow$	ERGAS $\downarrow$	SAM $\downarrow$
LTTR	35.9105	0.9534	2.5996	14.4999
LTMR	36.1927	0.9556	2.5026	13.7503
GTNN	35.8465	0.9486	2.6096	15.1712
CNMF	38.8291	0.9558	2.0359	13.6203
Hysure	40.8093	0.9594	1.8441	14.8049
NLSTF	34.2629	0.9361	3.1578	16.2967
CSTF	38.2946	0.9660	2.1279	12.2264
CTDF	37.0001	0.9106	2.3732	19.5667
JSSO	35.4651	0.9038	3.0848	19.6212
BGS-GTF	41.0662	0.9536	1.7415	15.0933
FCTN	40.7569	0.9474	1.9461	14.7243
<b>BFCTN</b>	<b>41.4712</b>	<b>0.9723</b>	<b>1.5288</b>	<b>10.4926</b>

As shown in Tab. VII, the PSNR difference among the three standard separable kernels (Average,  $G_{4 \times 4}$ , and  $G_{7 \times 7}$ ) is less than 0.7 dB, indicating consistent high performance under standard blurring. In contrast, the motion blur kernels ( $M_{30^\circ}$

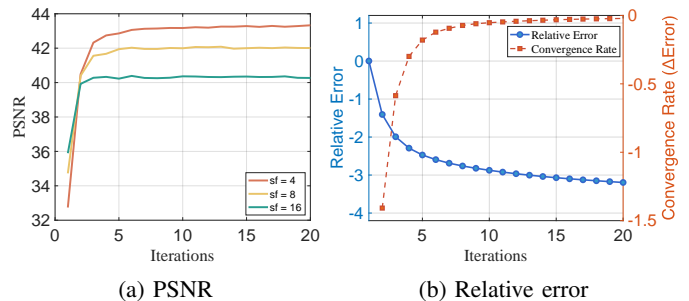


Fig. 13: The convergence behavior of the proposed method.

and  $M_{45^\circ}$ ) lead to a PSNR drop of more than 1 dB due to directional information loss during the SVD approximation. Notably, BFCTN outperforms competing methods under the motion blur condition (Tab. VIII), achieving a 20% relative improvement in SAM (from  $12.23^\circ$  to  $10.49^\circ$ ), it surpasses the fusion method BGS-GTF applicable to general spatial blurring. For the newly introduced complex kernels, including the elliptical Gaussian kernel ( $E_{30^\circ}$ ), the hybrid Gaussian-motion kernel ( $H_{G+M}$ ), and the channel-varying sensor-specific kernel ( $S_{\text{var}}$ ), only BFCTN results are reported due to computational constraints. Despite the increased difficulty of these degradations, BFCTN still achieves reasonable performance, demonstrating its robustness and adaptability. These results suggest that BFCTN can effectively handle a variety of separable and non-separable, directional, and heterogeneous degradations.

5) *Convergence Analysis*: Fig. 13 (a) illustrates the PSNR convergence process of the model under different downsampling factors. As the number of iterations increases, the PSNR gradually stabilizes. Fig. 13 (b) further analyzes the convergence characteristics at a downsampling factor of  $sf=4$ , where the relative error<sup>6</sup> and error convergence rate curves demonstrate that the error reduction diminishes significantly after five iterations, while the PSNR curve reaches a plateau. Both visual quality and numerical stability indicate that additional iterations yield negligible performance improvement. Based on these observations, the maximum number of iterations is empirically set to six in our implementation to balance efficiency and performance.

## V. CONCLUSION

This paper presents a hyperspectral-multispectral image fusion model, designated BFCTN, which is constructed on the foundation of Bayesian learning and the FCTN decomposition paradigm. By employing chunking and overlapping techniques, the model is able to efficiently extract the low-rank properties of the input images. Subsequently, We construct a fully connected tensor network structure by setting up a hierarchical sparse prior between factor tensors, which enables the model to take full advantage of the intrinsic structure of the data and the correlation between different dimensions.

<sup>6</sup>Relative error =  $\log(\|\mathcal{X}^{t+1} - \mathcal{X}^t\|_F / \|\mathcal{X}^t\|_F)$ , where  $\mathcal{X}^t$  and  $\mathcal{X}^{t+1}$  represent the previous iteration and the current result respectively. [33].

Furthermore, we develop a method for estimating model parameters using VB and EM, which effectively avoids the non-convex optimisation problem common to other fusion methods and greatly reduces the complexity of parameter selection. Extensive comparative experiments across multiple datasets and diverse input scenarios, the proposed BFCTN method demonstrates not only state-of-the-art fusion performance and remarkable robustness against strong noise interference and various degradation effects, but also demonstrates practical applicability on real datasets.

## REFERENCES

- [1] N. Yokoya, T. Yairi, and A. Iwasaki, "Coupled non-negative matrix factorization (cnmf) for hyperspectral and multispectral data fusion: Application to pasture classification," in *2011 IEEE International Geoscience and Remote Sensing Symposium*. IEEE, 2011, pp. 1779–1782.
- [2] M. Simoes, J. Bioucas-Dias, L. B. Almeida, and J. Chanussot, "Hyperspectral image super-resolution: An edge-preserving convex formulation," in *2014 IEEE International Conference on Image Processing (ICIP)*. IEEE, 2014, pp. 4166–4170.
- [3] R. Dian, L. Fang, and S. Li, "Hyperspectral image super-resolution via non-local sparse tensor factorization," in *Proceedings of the IEEE Conference on Computer Vision and Pattern Recognition*, 2017, pp. 5344–5353.
- [4] R. Dian, S. Li, L. Fang, T. Lu, and J. M. Bioucas-Dias, "Nonlocal sparse tensor factorization for semiblind hyperspectral and multispectral image fusion," *IEEE Transactions on Cybernetics*, vol. 50, no. 10, pp. 4469–4480, 2019.
- [5] S. Li, R. Dian, L. Fang, and J. M. Bioucas-Dias, "Fusing hyperspectral and multispectral images via coupled sparse tensor factorization," *IEEE Transactions on Image Processing*, vol. 27, no. 8, pp. 4118–4130, 2018.
- [6] R. Dian, S. Li, and L. Fang, "Learning a low tensor-train rank representation for hyperspectral image super-resolution," *IEEE Transactions on Neural Networks and Learning Systems*, vol. 30, no. 9, pp. 2672–2683, 2019.
- [7] R. Dian and S. Li, "Hyperspectral image super-resolution via subspace-based low tensor multi-rank regularization," *IEEE Transactions on Image Processing*, vol. 28, no. 10, pp. 5135–5146, 2019.
- [8] Y.-B. Zheng, T.-Z. Huang, X.-L. Zhao, Q. Zhao, and T.-X. Jiang, "Fully-connected tensor network decomposition and its application to higher-order tensor completion," in *Proceedings of the AAAI Conference on Artificial Intelligence*, vol. 35, no. 12, 2021, pp. 11 071–11 078.
- [9] T. G. Kolda and B. W. Bader, "Tensor decompositions and applications," *SIAM review*, vol. 51, no. 3, pp. 455–500, 2009.
- [10] F. Ye, Z. Wu, X. Jia, J. Chanussot, Y. Xu, and Z. Wei, "Bayesian nonlocal patch tensor factorization for hyperspectral image super-resolution," *IEEE Transactions on Image Processing*, 2023.
- [11] L. Cheng, X. Tong, S. Wang, Y.-C. Wu, and H. V. Poor, "Learning nonnegative factors from tensor data: Probabilistic modeling and inference algorithm," *IEEE Transactions on Signal Processing*, vol. 68, pp. 1792–1806, 2020.
- [12] X.-L. Meng and D. B. Rubin, "Maximum likelihood estimation via the ecm algorithm: A general framework," *Biometrika*, vol. 80, no. 2, pp. 267–278, 1993.
- [13] C. Zhang, J. Bütepage, H. Kjellström, and S. Mandt, "Advances in variational inference," *IEEE Transactions on Pattern Analysis and Machine Intelligence*, vol. 41, no. 8, pp. 2008–2026, 2018.
- [14] J. Zeng, G. Zhou, Y. Qiu, C. Li, and Q. Zhao, "Bayesian tensor network structure search and its application to tensor completion," *Neural Networks*, vol. 175, p. 106290, 2024.
- [15] Q. Zhao, L. Zhang, and A. Cichocki, "Bayesian cp factorization of incomplete tensors with automatic rank determination," *IEEE Transactions on Pattern Analysis and Machine Intelligence*, vol. 37, no. 9, pp. 1751–1763, 2015.
- [16] Q. Zhao, G. Zhou, L. Zhang, A. Cichocki, and S.-I. Amari, "Bayesian robust tensor factorization for incomplete multiway data," *IEEE Transactions on Neural Networks and Learning Systems*, vol. 27, no. 4, pp. 736–748, 2015.
- [17] V. Simoncini, "Computational methods for linear matrix equations," *siam REVIEW*, vol. 58, no. 3, pp. 377–441, 2016.
- [18] D. Jin, J. Liu, J. Yang, and Z. Wu, "High-order coupled fully connected tensor network decomposition for hyperspectral image super-resolution," *IEEE Geoscience and Remote Sensing Letters*, vol. 19, pp. 1–5, 2022.
- [19] T. Xu, T.-Z. Huang, L.-J. Deng, J.-L. Xiao, C. Broni-Bediako, J. Xia, and N. Yokoya, "A coupled tensor double-factor method for hyperspectral and multispectral image fusion," *IEEE Transactions on Geoscience and Remote Sensing*, 2024.
- [20] A. Guha, "Mineral exploration using hyperspectral data," in *Hyperspectral Remote Sensing*. Elsevier, 2020, pp. 293–318.
- [21] J. M. Bioucas-Dias, A. Plaza, G. Camps-Valls, P. Scheunders, N. Nasrabadi, and J. Chanussot, "Hyperspectral remote sensing data analysis and future challenges," *IEEE Geoscience and Remote Sensing Magazine*, vol. 1, no. 2, pp. 6–36, 2013.
- [22] M. B. Stuart, A. J. McGonigle, and J. R. Willmott, "Hyperspectral imaging in environmental monitoring: A review of recent developments and technological advances in compact field deployable systems," *Sensors*, vol. 19, no. 14, p. 3071, 2019.
- [23] B. Lu, P. D. Dao, J. Liu, Y. He, and J. Shang, "Recent advances of hyperspectral imaging technology and applications in agriculture," *Remote Sensing*, vol. 12, no. 16, p. 2659, 2020.
- [24] H. Petersson, D. Gustafsson, and D. Bergstrom, "Hyperspectral image analysis using deep learning—a review," in *2016 sixth international conference on image processing theory, tools and applications (IPTA)*. IEEE, 2016, pp. 1–6.
- [25] R. B. Gomez, A. Jazaeri, and M. Kafatos, "Wavelet-based hyperspectral and multispectral image fusion," in *Geo-Spatial Image and Data Exploitation II*, vol. 4383. SPIE, 2001, pp. 36–42.
- [26] L. Loncan, L. B. De Almeida, J. M. Bioucas-Dias, X. Briottet, J. Chanussot, N. Dobigeon, S. Fabre, W. Liao, G. A. Licciardi, M. Simoes *et al.*, "Hyperspectral pansharpening: A review," *IEEE Geoscience and Remote Sensing Magazine*, vol. 3, no. 3, pp. 27–46, 2015.
- [27] D. Sara, A. K. Mandava, A. Kumar, S. Duella, and A. Jude, "Hyperspectral and multispectral image fusion techniques for high resolution applications: A review," *Earth Science Informatics*, vol. 14, no. 4, pp. 1685–1705, 2021.
- [28] C. Wang, Y. Liu, X. Bai, W. Tang, P. Lei, and J. Zhou, "Deep residual convolutional neural network for hyperspectral image super-resolution," in *Image and Graphics: 9th International Conference, ICG 2017, Shanghai, China, September 13–15, 2017, Revised Selected Papers, Part III 9*. Springer, 2017, pp. 370–380.
- [29] X.-H. Han, Y. Zheng, and Y.-W. Chen, "Multi-level and multi-scale spatial and spectral fusion cnn for hyperspectral image super-resolution," in *Proceedings of the IEEE/CVF International Conference on Computer Vision Workshops*, 2019, pp. 0–0.
- [30] J. Xiao, J. Li, Q. Yuan, M. Jiang, and L. Zhang, "Physics-based gan with iterative refinement unit for hyperspectral and multispectral image fusion," *IEEE Journal of Selected Topics in Applied Earth Observations and Remote Sensing*, vol. 14, pp. 6827–6841, 2021.
- [31] X. He, Y. Chen, and P. Ghamisi, "Heterogeneous transfer learning for hyperspectral image classification based on convolutional neural network," *IEEE Transactions on Geoscience and Remote Sensing*, vol. 58, no. 5, pp. 3246–3263, 2019.
- [32] X. X. Zhu, D. Tuija, L. Mou, G.-S. Xia, L. Zhang, F. Xu, and F. Fraundorfer, "Deep learning in remote sensing: A comprehensive review and list of resources," *IEEE Geoscience and Remote Sensing Magazine*, vol. 5, no. 4, pp. 8–36, 2017.
- [33] Y. Zhou and Y.-M. Cheung, "Bayesian low-tubal-rank robust tensor factorization with multi-rank determination," *IEEE Transactions on Pattern Analysis and Machine Intelligence*, vol. 43, no. 1, pp. 62–76, 2019.
- [34] Y. Wang, W. Li, N. Liu, Y. Gui, and R. Tao, "Fubay: An integrated fusion framework for hyperspectral super-resolution based on bayesian tensor ring," *IEEE Transactions on Neural Networks and Learning Systems*, 2023.
- [35] L. Wald, T. Ranchin, and M. Mangolini, "Fusion of satellite images of different spatial resolutions: Assessing the quality of resulting images," *Photogrammetric Engineering and Remote Sensing*, vol. 63, no. 6, pp. 691–699, 1997.
- [36] Y. Chen, W. Lai, W. He, X.-L. Zhao, and J. Zeng, "Hyperspectral compressive snapshot reconstruction via coupled low-rank subspace representation and self-supervised deep network," *IEEE Transactions on Image Processing*, 2024.
- [37] S. Hajaj, A. El Harti, A. B. Pour, A. Jellouli, Z. Adiri, and M. Hashim, "A review on hyperspectral imagery application for lithological mapping and mineral prospecting: Machine learning techniques and future prospects," *Remote Sensing Applications: Society and Environment*, p. 101218, 2024.
- [38] J. G. A. Barbedo, "A review on the combination of deep learning techniques with proximal hyperspectral images in agriculture," *Computers and Electronics in Agriculture*, vol. 210, p. 107920, 2023.

- [39] Y. Tang, S. Song, S. Gui, W. Chao, C. Cheng, and R. Qin, "Active and low-cost hyperspectral imaging for the spectral analysis of a low-light environment," *Sensors*, vol. 23, no. 3, p. 1437, 2023.
- [40] R. Dian, Y. Liu, and S. Li, "Hyperspectral image fusion via a novel generalized tensor nuclear norm regularization," *IEEE Transactions on Neural Networks and Learning Systems*, 2024.
- [41] M. Simoes, J. Bioucas-Dias, L. B. Almeida, and J. Chanussot, "A convex formulation for hyperspectral image superresolution via subspace-based regularization," *IEEE Transactions on Geoscience and Remote Sensing*, vol. 53, no. 6, pp. 3373–3388, 2014.
- [42] R. Dian, A. Guo, and S. Li, "Zero-shot hyperspectral sharpening," *IEEE Transactions on Pattern Analysis and Machine Intelligence*, vol. 45, no. 10, pp. 12 650–12 666, 2023.
- [43] J. Li, K. Zheng, L. Gao, L. Ni, M. Huang, and J. Chanussot, "Model-informed multi-stage unsupervised network for hyperspectral image super-resolution," *IEEE Transactions on Geoscience and Remote Sensing*, 2024.
- [44] J. Li, K. Zheng, L. Gao, Z. Han, Z. Li, and J. Chanussot, "Enhanced deep image prior for unsupervised hyperspectral image super-resolution," *IEEE Transactions on Geoscience and Remote Sensing*, 2025.
- [45] Y. Liu, R. Dian, and S. Li, "Low-rank transformer for high-resolution hyperspectral computational imaging," *International Journal of Computer Vision*, vol. 133, no. 2, pp. 809–824, 2025.
- [46] J. Long, Y. Zhan, Z. Pang, T. Zhou, X. Li, L. Lan, and Y. Peng, "Joint spatial-spectral optimization for the high-magnification fusion of hyperspectral and multispectral images," *IEEE Transactions on Geoscience and Remote Sensing*, 2024.
- [47] Y. Wang, W. Li, Y. Gui, Q. Du, and J. E. Fowler, "A generalized tensor formulation for hyperspectral image super-resolution under general spatial blurring," *IEEE Transactions on Pattern Analysis and Machine Intelligence*, 2025.
- [48] Z. Yang, L. T. Yang, H. Wang, H. Zhao, and D. Liu, "Bayesian non-negative tensor completion with automatic rank determination," *IEEE Transactions on Image Processing*, 2025.
- [49] J. Xue, Y. Zhao, Y. Bu, J. C.-W. Chan, and S. G. Kong, "When laplacian scale mixture meets three-layer transform: A parametric tensor sparsity for tensor completion," *IEEE Transactions on Cybernetics*, vol. 52, no. 12, pp. 13 887–13 901, 2022.
- [50] J. Xue, Y. Zhao, S. Huang, W. Liao, J. C.-W. Chan, and S. G. Kong, "Multilayer sparsity-based tensor decomposition for low-rank tensor completion," *IEEE Transactions on Neural Networks and Learning Systems*, vol. 33, no. 11, pp. 6916–6930, 2021.
- [51] J. Xue, Y. Zhao, T. Wu, and J. C.-W. Chan, "Tensor convolution-like low-rank dictionary for high-dimensional image representation," *IEEE Transactions on Circuits and Systems for Video Technology*, 2024.
- [52] L. Wald, "Quality of high resolution synthesised images: Is there a simple criterion?" in *Third conference" Fusion of Earth data: merging point measurements, raster maps and remotely sensed images"*. SEE/URISCA, 2000, pp. 99–103.
- [53] N. Yokoya, C. Grohnfeldt, and J. Chanussot, "Hyperspectral and multispectral data fusion: A comparative review of the recent literature," *IEEE Geoscience and Remote Sensing Magazine*, vol. 5, no. 2, pp. 29–56, 2017.
- [54] J. K. Kruschke, "Bayesian data analysis," *Wiley interdisciplinary reviews: cognitive science*, vol. 1, no. 5, pp. 658–676, 2010.
- [55] H. Wang, Y. Xu, Z. Wu, and Z. Wei, "Unsupervised hyperspectral and multispectral image blind fusion based on deep tucker decomposition network with spatial-spectral manifold learning," *IEEE Transactions on Neural Networks and Learning Systems*, 2024.
- [56] R. Dian, T. Shan, W. He, and H. Liu, "Spectral super-resolution via model-guided cross-fusion network," *IEEE Transactions on Neural Networks and Learning Systems*, vol. 35, no. 7, pp. 10 059–10 070, 2023.
- [57] R. Dian, Y. Liu, and S. Li, "Spectral super-resolution via deep low-rank tensor representation," *IEEE Transactions on Neural Networks and Learning Systems*, vol. 36, no. 3, pp. 5140–5150, 2024.
- [58] X. Cao, Y. Lian, J. Li, K. Wang, and C. Ma, "Unsupervised multi-level spatio-spectral fusion transformer for hyperspectral image super-resolution," *Optics & Laser Technology*, vol. 176, p. 111032, 2024.
- [59] X. Cao, Y. Lian, K. Wang, C. Ma, and X. Xu, "Unsupervised hybrid network of transformer and cnn for blind hyperspectral and multispectral image fusion," *IEEE Transactions on Geoscience and Remote Sensing*, vol. 62, pp. 1–15, 2024.
- [60] X. Tian, W. Zhang, D. Yu, and J. Ma, "Sparse tensor prior for hyperspectral, multispectral, and panchromatic image fusion," *IEEE/CAA Journal of Automatica Sinica*, vol. 10, no. 1, pp. 284–286, 2022.

## APPENDIX

A. The posterior estimation of factor tensors  $\mathcal{T}_n^k$ .

- 1) The posterior estimation of  $\mathcal{T}_1^k$ : The estimation of  $\mathcal{T}_1^k$  is presented in Sec. III. B of the paper (main document).
- 2) The posterior estimation of  $\mathcal{T}_2^k$ : For  $\mathcal{T}_2^k$ , the optimization objective function is

$$\begin{aligned} \max \mathbb{E}_{q(\Xi^k \setminus \mathcal{T}_2^k)} \left\{ -\frac{\tau_h^k}{2} \|\mathcal{H}^k - \text{FCTN}(\mathcal{T}_1^k \times_1 \mathbf{P}_1, \mathcal{T}_2^k \times_2 \mathbf{P}_2, \mathcal{T}_3^k, \mathcal{T}_4^k)\|_{\text{F}}^2 \right. \\ \left. - \frac{\tau_m^k}{2} \|\mathcal{M}^k - \text{FCTN}(\mathcal{T}_1^k, \mathcal{T}_2^k, \mathcal{T}_3^k \times_3 \mathbf{P}_3, \mathcal{T}_4^k)\|_{\text{F}}^2 - \frac{1}{2} \text{Tr} \left( \mathbf{T}_{2(2)}^k \mathbf{\Lambda}_2^k \mathbf{T}_{2(2)}^{k \top} \right) \right\} \end{aligned}$$

According to the EM rule, optimizing the above formula can obtain a Sylvette equation as follows:

$$\begin{aligned} \mathbf{T}_{2(2)}^k \left\{ \mathbb{E}[\tau_m^k] \mathbb{E}[\mathbf{M}_{\neq 2}^k \mathbf{M}_{\neq 2}^{k \top}] + \mathbb{E}[\mathbf{\Lambda}_2^k] \right\} + \mathbb{E}[\tau_h^k] \mathbf{P}_2 \mathbf{P}_2 \mathbf{T}_{2(2)}^k \mathbb{E}[\mathbf{H}_{\neq 2}^k \mathbf{H}_{\neq 2}^{k \top}] \\ = \mathbb{E}[\tau_m^k] \mathbf{M}_{(2)}^k \mathbb{E}[\mathbf{M}_{\neq 2}^k \mathbf{M}_{\neq 2}^{k \top}] + \mathbb{E}[\tau_h^k] \mathbf{P}_2 \mathbf{H}_{(2)}^k \mathbb{E}[\mathbf{H}_{\neq 2}^k \mathbf{H}_{\neq 2}^{k \top}]. \end{aligned}$$

Here,  $\mathbf{T}_{2(2)}^k$  is regarded as the  $X$  variable, and solving the Sylvette equation of the form  $\mathbf{A}\mathbf{X}\mathbf{B} + \mathbf{C}\mathbf{X}\mathbf{D} = \mathbf{E}$  can yield the estimated value of  $\mathbf{T}_{2(2)}^k$ . Further folding of  $\mathbf{T}_{2(2)}^k$  is the estimated value of  $\mathcal{T}_2^k$ .

- 3) The posterior estimation of  $\mathcal{T}_3^k$ : For  $\mathcal{T}_3^k$ , the optimization problem of the model is

$$\begin{aligned} \max \mathbb{E}_{q(\Xi^k \setminus \mathcal{T}_3^k)} \left\{ -\frac{\tau_h^k}{2} \|\mathcal{H}^k - \text{FCTN}(\mathcal{T}_1^k \times_1 \mathbf{P}_1, \mathcal{T}_2^k \times_2 \mathbf{P}_2, \mathcal{T}_3^k, \mathcal{T}_4^k)\|_{\text{F}}^2 \right. \\ \left. - \frac{\tau_m^k}{2} \|\mathcal{M}^k - \text{FCTN}(\mathcal{T}_1^k, \mathcal{T}_2^k, \mathcal{T}_3^k \times_3 \mathbf{P}_3, \mathcal{T}_4^k)\|_{\text{F}}^2 - \frac{1}{2} \text{Tr} \left( \mathbf{T}_{3(3)}^k \mathbf{\Lambda}_3^k \mathbf{T}_{3(3)}^{k \top} \right) \right\} \end{aligned}$$

Similarly, the estimation of  $\mathcal{T}_3^k$  can be obtained by solving the following linear system

$$\begin{aligned} \mathbf{T}_{3(3)}^k \left\{ \mathbb{E}[\tau_h^k] \mathbb{E}[\mathbf{H}_{\neq 3}^k \mathbf{H}_{\neq 3}^{k \top}] + \mathbb{E}[\mathbf{\Lambda}_3^k] \right\} + \mathbb{E}[\tau_m^k] \mathbf{P}_3 \mathbf{P}_3 \mathbf{T}_{3(3)}^k \mathbb{E}[\mathbf{M}_{\neq 3}^k \mathbf{M}_{\neq 3}^{k \top}] \\ = \mathbb{E}[\tau_m^k] \mathbf{P}_3 \mathbf{M}_{(3)}^k \mathbb{E}[\mathbf{M}_{\neq 3}^k \mathbf{M}_{\neq 3}^{k \top}] + \mathbb{E}[\tau_h^k] \mathbf{H}_{(3)}^k \mathbb{E}[\mathbf{H}_{\neq 3}^k \mathbf{H}_{\neq 3}^{k \top}]. \end{aligned}$$

- 4) The posterior estimation of  $\mathcal{T}_4^k$ : For  $\mathcal{T}_4^k$ , the optimization problem of the model is

$$\begin{aligned} \max \mathbb{E}_{q(\Xi^k \setminus \mathcal{T}_4^k)} \left\{ -\frac{\tau_h^k}{2} \|\mathcal{H}^k - \text{FCTN}(\mathcal{T}_1^k \times_1 \mathbf{P}_1, \mathcal{T}_2^k \times_2 \mathbf{P}_2, \mathcal{T}_3^k, \mathcal{T}_4^k)\|_{\text{F}}^2 \right. \\ \left. - \frac{\tau_m^k}{2} \|\mathcal{M}^k - \text{FCTN}(\mathcal{T}_1^k, \mathcal{T}_2^k, \mathcal{T}_3^k \times_3 \mathbf{P}_3, \mathcal{T}_4^k)\|_{\text{F}}^2 - \frac{1}{2} \text{Tr} \left( \mathbf{T}_{4(4)}^k \mathbf{\Lambda}_4^k \mathbf{T}_{4(4)}^{k \top} \right) \right\} \end{aligned}$$

Similarly, the estimation of  $\mathcal{T}_4^k$  can be obtained by solving the following linear system

$$\mathbf{T}_{4(4)}^k \mathbb{E} \left\{ [\tau_h^k] \mathbb{E}[\mathbf{H}_{\neq 4}^k \mathbf{H}_{\neq 4}^{k \top}] + \mathbb{E}[\tau_m^k] \mathbb{E}[\mathbf{M}_{\neq 4}^k \mathbf{M}_{\neq 4}^{k \top}] + \mathbb{E}[\mathbf{\Lambda}_4^k] \right\} = \mathbb{E}[\tau_h^k] \mathbf{H}_{(4)}^k \mathbb{E}[\mathbf{H}_{\neq 4}^k \mathbf{H}_{\neq 4}^{k \top}] + \mathbb{E}[\tau_m^k] \mathbf{M}_{(4)}^k \mathbb{E}[\mathbf{M}_{\neq 4}^k \mathbf{M}_{\neq 4}^{k \top}].$$

### B. The posterior distribution of $\lambda^{(n_1, n_2)}$

$$\begin{aligned}
q\left(\lambda_{(n_1, n_2)}^k\right) &\propto \exp\left\{\mathbb{E}_q(\Xi - \lambda_{(n_1, n_2)}^k) \left[\ln \mathcal{L}\left(\mathbf{T}_{n_1}^k, \mathbf{T}_{n_2}^k \mid \Lambda_{n_1}^k, \Lambda_{n_2}^k\right) + \ln p\left(\lambda_{(n_1, n_2)}^k \mid a_0, b_0\right)\right]\right\} \\
&\propto \prod_r^{R_{n_1, n_2}} \exp\left\{\mathbb{E}_q\left[\frac{1}{2} \ln \left|\Lambda_{n_1}^k\right| - \frac{1}{2} \mathbf{T}_{n_1(n_2)}^k(r)^\top \Lambda_{n_1}^k \mathbf{T}_{n_1(n_2)}^k(r)\right.\right. \\
&\quad \left.\left. + \frac{1}{2} \ln \left|\Lambda_{n_2}^k\right| - \frac{1}{2} \mathbf{T}_{n_2(n_1)}^k(r)^\top \Lambda_{n_2}^k \mathbf{T}_{n_2(n_1)}^k(r) + (a_0 - 1) \ln(\lambda_{n_1, n_2}^k)_r - b_0(\lambda_{n_1, n_2}^k)_r\right]\right\} \\
&\propto \prod_r^{R_{n_1, n_2}} \exp\left\{\mathbb{E}_q\left[\left(a_0 + \frac{I_{n_1} \prod_{n \neq n_1, n_2}^N R_{n, n_1} + I_{n_2} \prod_{n \neq n_1, n_2}^N R_{n, n_2}}{2} - 1\right) \ln(\lambda_{n_1, n_2}^k)_r\right.\right. \\
&\quad \left.\left. - \left(b_0 + \frac{1}{2} \left(\lambda_{n_1, \neq n_2}^k \mathbf{T}_{n_1(n_2)}^k(r)^2 + \lambda_{n_2, \neq n_1}^k \mathbf{T}_{n_2(n_1)}^k(r)^2\right)\right) (\lambda_{n_1, n_2}^k)_r\right]\right\} \\
&\propto \prod_r^{R_{n_1, n_2}} (\lambda_{n_1, n_2}^k)_r^{a_0 + \frac{I_{n_1} \prod_{n \neq n_1, n_2}^N R_{n, n_1} + I_{n_2} \prod_{n \neq n_1, n_2}^N R_{n, n_2}}{2} - 1} \\
&\quad \cdot \exp\left\{-\left(b_0 + \frac{1}{2} \left(\mathbb{E}_q\left[\mathbf{T}_{n_1(n_2)}^k(r)^\top \lambda_{n_1, \neq n_2}^k \mathbf{T}_{n_1(n_2)}^k(r)\right] + \mathbb{E}_q\left[\mathbf{T}_{n_2(n_1)}^k(r)^\top \lambda_{n_2, \neq n_1}^k \mathbf{T}_{n_2(n_1)}^k(r)\right]\right) (\lambda_{n_1, n_2}^k)_r\right\} \\
&\propto \prod_r^{R_{n_1, n_2}} \text{Ga}\left((\lambda_{n_1, n_2}^k)_r \mid a_{n_1, n_2}^k, b_{n_1, n_2}^k\right)
\end{aligned}$$

Therefore, the posterior of  $\lambda^{(n_1, n_2)}$  also follows the gamma distribution, and the posterior parameters can be obtained from the above form, where

$$\begin{aligned}
a_{n_1, n_2}^k &= a_0 + \frac{I_{n_1} \prod_{n \neq n_1, n_2}^N R_{n, n_1} + I_{n_2} \prod_{n \neq n_1, n_2}^N R_{n, n_2}}{2} \\
b_{n_1, n_2}^k &= b_0 + \frac{1}{2} \left(\mathbb{E}_q\left[\mathbf{T}_{n_1(n_2)}^k(r)^\top \lambda_{n_1, \neq n_2}^k \mathbf{T}_{n_1(n_2)}^k(r)\right] + \mathbb{E}_q\left[\mathbf{T}_{n_2(n_1)}^k(r)^\top \lambda_{n_2, \neq n_1}^k \mathbf{T}_{n_2(n_1)}^k(r)\right]\right).
\end{aligned}$$

### C. The posterior distribution of $\tau_h^k$

$$\begin{aligned}
q\left(\tau_h^k\right) &\propto \exp\left\{\mathbb{E}_q(\Xi - \tau_h^k) \left[\ln \mathcal{L}\left(\mathcal{H}^k \mid \{\mathcal{T}_n^k\}_{n=1}^4, \tau_h^k\right) + \ln p\left(\tau_h^k\right)\right]\right\} \\
&\propto \exp\left\{\mathbb{E}_q\left[\ln\left(\tau_h^k \frac{I_1' I_2' I_3 I_4}{2}\right) - \frac{\tau_h^k}{2} \sum_{i_1'}^{I_1'} \sum_{i_2}^{I_2'} \sum_{i_3}^{I_3} \sum_{i_4}^{I_4} \left(\mathcal{H}_{i_1' i_2' i_3 i_4}^k - \hat{\mathcal{H}}_{i_1' i_2' i_3 i_4}^k\right)^2 + \ln\left(\tau_h^{k c_0 - 1}\right) - d_0 \tau_h^k\right]\right\} \\
&\propto \tau_h^{k c_0 + \frac{I_1' I_2' I_3 I_4}{2} - 1} \exp\left\{-\left(d_0 + \frac{1}{2} \mathbb{E}_q\left[\left\|\left(\mathcal{H}^k - \hat{\mathcal{H}}^k\right)\right\|_F^2\right]\right) \tau_h^k\right\} \\
&\propto \tau_h^{k c_0 + \frac{I_1' I_2' I_3 I_4}{2} - 1} \exp\left\{-\left(d_0 + \frac{1}{2} \mathbb{E}_q\left[\left\|\left(\mathcal{H}^k - \text{FCTN}\left(\mathcal{T}_1^k \times_1 \mathbf{P}_1, \mathcal{T}_2^k \times_2 \mathbf{P}_2, \mathcal{T}_3^k, \mathcal{T}_4^k\right)\right)\right\|_F^2\right]\right) \tau_h^k\right\} \\
&\propto \text{Ga}\left(\tau_h^k \mid c^k, d^k\right)
\end{aligned}$$

Thus, the posterior of  $\tau_h^k$  is a parametric updated Gamma distribution, where the parameters are updated according to the following rule:

$$\begin{aligned}
c^k &= c_0 + \frac{I_1' I_2' I_3 I_4}{2} \\
d^k &= d_0 + \frac{1}{2} \mathbb{E}_q\left[\left\|\left(\mathcal{H}^k - \text{FCTN}\left(\mathcal{T}_1^k \times_1 \mathbf{P}_1, \mathcal{T}_2^k \times_2 \mathbf{P}_2, \mathcal{T}_3^k, \mathcal{T}_4^k\right)\right)\right\|_F^2\right].
\end{aligned}$$

#### D. The posterior distribution of $\tau_m^k$

$$\begin{aligned}
q(\tau_m^k) &\propto \exp \left\{ \mathbb{E}_q(\Xi^{-\tau_m^k}) \left[ \ln \mathcal{L}(\mathcal{M}^k | \{\mathcal{T}_n^k\}_{n=1}^4, \tau_m^k) + \ln p(\tau_m^k) \right] \right\} \\
&\propto \exp \left\{ \mathbb{E}_q \left[ \ln \left( \tau_m^k \frac{I_1 I_2 I_3' I_4}{2} \right) - \frac{\tau_m^k}{2} \sum_{i_1}^{I_1} \sum_{i_2}^{I_2} \sum_{i_3'}^{I_3'} \sum_{i_4}^{I_4} \left( \mathcal{M}_{i_1 i_2 i_3' i_4}^k - \hat{\mathcal{M}}_{i_1 i_2 i_3' i_4}^k \right)^2 + \ln \left( \tau_m^k e_0^{-1} \right) - f_0 \tau_m^k \right] \right\} \\
&\propto \tau_m^k e_0 + \frac{I_1 I_2 I_3' I_4}{2} - 1 \exp \left\{ - \left( f_0 + \frac{1}{2} \mathbb{E}_q \left[ \left\| (\mathcal{M}^k - \hat{\mathcal{M}}^k) \right\|_F^2 \right] \right) \tau_m^k \right\} \\
&\propto \tau_m^k e_0 + \frac{I_1 I_2 I_3' I_4}{2} - 1 \exp \left\{ - \left( f_0 + \frac{1}{2} \mathbb{E}_q \left[ \left\| (\mathcal{M}^k - \text{FCTN}(\mathcal{T}_1^k, \mathcal{T}_2^k, \mathcal{T}_3^k \times_3 \mathbf{P}_3, \mathcal{T}_4^k)) \right\|_F^2 \right] \right) \tau_m^k \right\} \\
&\propto \text{Ga}(\tau_m^k | e^k, f^k)
\end{aligned}$$

Similarly, the posterior of  $\tau_m^k$  is a parametric updated Gamma distribution, where the parameters are updated according to the following rule:

$$\begin{aligned}
e^k &= e_0 + \frac{I_1 I_2 I_3' I_4}{2} \\
f^k &= f_0 + \frac{1}{2} \mathbb{E}_q \left[ \left\| (\mathcal{M}^k - \text{FCTN}(\mathcal{T}_1^k, \mathcal{T}_2^k, \mathcal{T}_3^k \times_3 \mathbf{P}_3, \mathcal{T}_4^k)) \right\|_F^2 \right].
\end{aligned}$$

#### E. Lower bound of model evidence

$$\begin{aligned}
ELBO &= \mathbb{E}_{q(\Xi^k)} [\ln p(\mathcal{H}^k, \mathcal{M}^k, \Xi^k)] + H(q(\Xi^k)) \\
&= \mathbb{E}_q(\{\mathcal{T}_n^{(k)}\}_{n=1}^4, \tau_h^k) \left[ \ln p(\mathcal{H}^k | \{\mathcal{T}_n^k\}_{n=1}^4, \tau_h^k) \right] + \mathbb{E}_q(\{\mathcal{T}_n^{(k)}\}_{n=1}^4, \tau_m^k) \left[ \ln p(\mathcal{M}^k | \{\mathcal{T}_n^k\}_{n=1}^4, \tau_m^k) \right] \\
&+ \mathbb{E}_q(\{\mathcal{T}_n^k\}_{n=1}^4) \left[ \sum_{n=1}^4 \ln p(\mathcal{T}_n^k | \lambda_{1,n}^k, \dots, \lambda_{n-1,n}^k, \lambda_{n,n+1}^k, \dots, \lambda_{n,N}^k) \right] + \mathbb{E}_{q(\lambda_{n_1, n_2}^k)} \left[ \sum_{n_1=1}^3 \sum_{n_2=n_1+1}^4 \ln p(\lambda_{n_1, n_2}^k) \right] \\
&+ \mathbb{E}_{q(\tau_h^k)} [\ln p(\tau_h^k)] + \mathbb{E}_{q(\tau_m^k)} [\ln p(\tau_m^k)] - \mathbb{E}_q(\{\mathcal{T}_n^{(k)}\}_{n=1}^4) \left[ \sum_{n=1}^4 \ln q(\mathcal{T}_n^{(k)}) \right] - \mathbb{E}_{q(\lambda_{n_1, n_2}^k)} \left[ \sum_{n_1=1}^3 \sum_{n_2=n_1+1}^4 \ln q(\lambda_{n_1, n_2}^k) \right] \\
&- \mathbb{E}_{q(\tau_h^k)} [\ln q(\tau_h^k)] - \mathbb{E}_{q(\tau_m^k)} [\ln q(\tau_m^k)]
\end{aligned}$$

The evidence lower bound of model consists of  $\mathbb{E}_{q(\Xi^k)} [\ln p(\mathcal{H}^k, \mathcal{M}^k, \Xi^k)]$  and  $H(q(\Xi^k))$ , the former is the expectation of the log prior distribution of the parameter and the latter is the entropy of the posterior distribution of the parameter, where:

$$\begin{aligned}
&\mathbb{E}_q \left[ \ln p \left( \mathcal{H}^k | \{\mathcal{T}_n^k\}_{n=1}^4, \tau_h^k \right) \right] \\
&= - \frac{I_1' I_2' I_3' I_4}{2} (\ln(2\pi) - \mathbb{E}_q[\ln \tau_h^k]) - \frac{1}{2} \mathbb{E}_q[\tau_h^k] \mathbb{E}_q \left[ \left\| \mathcal{H}^k - \text{FCTN}(\mathcal{T}_1^k \times_1 \mathbf{P}_1, \mathcal{T}_2^k \times_2 \mathbf{P}_2, \mathcal{T}_3^k, \mathcal{T}_4^k) \right\|_F^2 \right] \\
&= \frac{I_1' I_2' I_3' I_4}{2} (\psi(c^k) - \ln d^k) - \frac{c^k}{2d^k} \mathbb{E}_q \left[ \left\| \mathcal{H}^k - \text{FCTN}(\mathcal{T}_1^k \times_1 \mathbf{P}_1, \mathcal{T}_2^k \times_2 \mathbf{P}_2, \mathcal{T}_3^k, \mathcal{T}_4^k) \right\|_F^2 \right] + C
\end{aligned}$$

$$\begin{aligned}
&\mathbb{E}_q \left[ \ln p \left( \mathcal{M}^k | \{\mathcal{T}_n^k\}_{n=1}^4, \tau_m^k \right) \right] \\
&= - \frac{I_1 I_2 I_3' I_4}{2} \left( \ln(2\pi) - \frac{1}{2} \mathbb{E}_q[\ln \tau_m^k] \right) - \frac{1}{2} \mathbb{E}_q[\tau_m^k] \mathbb{E}_q \left[ \left\| \mathcal{M}^k - \text{FCTN}(\mathcal{T}_1^k, \mathcal{T}_2^k, \mathcal{T}_3^k \times_3 \mathbf{P}_3, \mathcal{T}_4^k) \right\|_F^2 \right] \\
&= \frac{I_1 I_2 I_3' I_4}{2} (\psi(e^k) - \ln f^k) - \frac{e^k}{2f^k} \mathbb{E}_q \left[ \left\| \mathcal{M}^k - \text{FCTN}(\mathcal{T}_1^k, \mathcal{T}_2^k, \mathcal{T}_3^k \times_3 \mathbf{P}_3, \mathcal{T}_4^k) \right\|_F^2 \right] + C
\end{aligned}$$

$$\begin{aligned}
& \mathbb{E}_q \left[ \sum_{n=1}^4 \ln p \left( \mathcal{T}_n^k \mid \boldsymbol{\lambda}_{1,n}^k, \dots, \boldsymbol{\lambda}_{n-1,n}^k, \boldsymbol{\lambda}_{n,n+1}^k, \dots, \boldsymbol{\lambda}_{n,N}^k \right) \right] \\
&= \mathbb{E}_q \left[ \sum_{n=1}^4 \sum_{i_n}^{I_n} \left\{ \frac{1}{2} \ln \left| \boldsymbol{\Lambda}_n^k \right| - \frac{1}{2} \mathbf{T}_n^k(i_n)^\top \boldsymbol{\Lambda}_n^k \mathbf{T}_n^k(i_n) \right\} \right] + C \\
&= \sum_{n=1}^4 \left\{ \frac{I_n}{2} \left( \sum_r^{R_{1,n}} \mathbb{E}_q[\ln \lambda_{1,n}^k] + \dots + \sum_r^{R_{n-1,n}} \mathbb{E}_q[\ln \lambda_{n-1,n}^k] + \dots + \sum_r^{R_{n,4}} \mathbb{E}_q[\ln \lambda_{n,4}^k] \right) - \frac{1}{2} \sum_{i_n}^{I_n} \mathbb{E}_q \left[ \mathbf{T}_n^k(i_n)^\top \boldsymbol{\Lambda}_n^k \mathbf{T}_n^k(i_n) \right] \right\} + C \\
&= \frac{\sum_n I_n}{2} \left( \sum_r^{R_{1,n}} \mathbb{E}_q[\ln \lambda_{1,n}^k] + \dots + \sum_r^{R_{n-1,n}} \mathbb{E}_q[\ln \lambda_{n-1,n}^k] + \dots + \sum_r^{R_{n,4}} \mathbb{E}_q[\ln \lambda_{n,4}^k] \right) \\
&\quad - \frac{1}{2} \sum_{n=1}^4 \sum_{i_n}^{I_n} \left\{ \text{Tr} \left( \mathbb{E}_q[\boldsymbol{\Lambda}_n^k] \text{Var} \left( \mathbf{T}_n^k(i_n) \right) \right) + \mathbb{E}_q \left[ \mathbf{T}_n^k(i_n)^\top \right] \mathbb{E}_q[\boldsymbol{\Lambda}_n^k] \mathbb{E}_q \left[ \mathbf{T}_n^k(i_n) \right] \right\} + C \\
&= \frac{\sum_n I_n}{2} \left( \sum_r^{R_{1,n}} \left( \psi(a_{1,n}^k) - \ln b_{1,n}^k \right) + \sum_r^{R_{n-1,n}} \left( \psi(a_{n-1,n}^k) - \ln b_{n-1,n}^k \right) + \sum_r^{R_{n,4}} \left( \psi(a_{n,4}^k) - \ln b_{n,4}^k \right) \right) \\
&\quad - \frac{1}{2} \sum_{n=1}^4 \text{Tr} \left\{ \mathbb{E}_q[\boldsymbol{\Lambda}_n^k] \left( \mathbf{T}_{n(n)}^k \right)^\top \mathbf{T}_{n(n)}^k \right\} + C \\
&= \sum_{n_1=1}^3 \sum_{n_2=2}^4 \sum_r^{R_{n_1,n_2}} I_{n_1,n_2} \left( \psi(a_{n_1,n_2}^k) - \ln b_{n_1,n_2}^k \right) - \frac{1}{2} \sum_{n=1}^4 \text{Tr} \left\{ \mathbb{E}_q[\boldsymbol{\Lambda}_n^k] \left( \mathbf{T}_{n(n)}^k \right)^\top \mathbf{T}_{n(n)}^k \right\} + C
\end{aligned}$$

$$\begin{aligned}
& \mathbb{E}_q \left[ \sum_{n_1=1}^3 \sum_{n_2=2}^4 \ln p \left( \boldsymbol{\lambda}_{n_1,n_2}^k \right) \right] \\
&= \sum_{n_1=1}^3 \sum_{n_2=2}^4 \sum_r^{R_{n_1,n_2}} \left\{ -\ln \Gamma(a_0^k) + a_0^k \ln d_0^k + (c_0^k - 1) \mathbb{E}_q \left[ \ln \boldsymbol{\lambda}_{n_1,n_2}^k \right] - d_0^k \mathbb{E}_q \left[ \boldsymbol{\lambda}_{n_1,n_2}^k \right] \right\} \\
&= \sum_{n_1=1}^3 \sum_{n_2=2}^4 \sum_r^{R_{n_1,n_2}} \left\{ -\ln \Gamma(a_0^k) + a_0^k \ln b_0^k + (a_0^k - 1) \left( \psi(a_{n_1,n_2}^k) - \ln b_{n_1,n_2}^k \right) - b_0^k \frac{a_{n_1,n_2}^k}{b_{n_1,n_2}^k} \right\} \\
&\quad \mathbb{E}_q[\ln p(\tau_h^k)] = -\ln \Gamma(c_0^k) + c_0^k \ln d_0^k + (c_0^k - 1) \mathbb{E}_q[\ln \tau] - d_0^k \mathbb{E}_q[\tau_h^k] \\
&\quad \quad \quad = -\ln \Gamma(c_0^k) + c_0^k \ln d_0^k + (c_0^k - 1) \left( \psi(c^k) - \ln d^k \right) - d_0^k \frac{c^k}{d^k} \\
&\quad \mathbb{E}_q[\ln p(\tau_m^k)] = -\ln \Gamma(e_0^k) + e_0^k \ln f_0^k + (e_0^k - 1) \mathbb{E}_q[\ln \tau] - f_0^k \mathbb{E}_q[\tau_m^k] \\
&\quad \quad \quad = -\ln \Gamma(e_0^k) + e_0^k \ln f_0^k + (e_0^k - 1) \left( \psi(e^k) - \ln f^k \right) - f_0^k \frac{e^k}{f^k} \\
&\quad -\mathbb{E}_q \left[ \sum_{n_1=1}^3 \sum_{n_2=2}^4 \ln q \left( \boldsymbol{\lambda}_{n_1,n_2}^k \right) \right] = \sum_{n_1=1}^3 \sum_{n_2=2}^4 \sum_r^{R_{n_1,n_2}} \left\{ \ln \Gamma(a_{n_1,n_2}^k) - (a_{n_1,n_2}^k - 1) \psi(a_{n_1,n_2}^k) - \ln b_{n_1,n_2}^k + a_{n_1,n_2}^k \right\} \\
&\quad \quad \quad -\mathbb{E}_q \left[ \ln q(\tau_h^k) \right] = \ln \Gamma(c^k) - (c^k - 1) \psi(c^k) - \ln d^k + c^k \\
&\quad \quad \quad -\mathbb{E}_q \left[ \ln q(\tau_m^k) \right] = \ln \Gamma(e^k) - (e^k - 1) \psi(e^k) - \ln f^k + e^k
\end{aligned}$$

In the above formula derivation,  $\psi(\cdot)$  denotes the digamma function and  $\Gamma(\cdot)$  denotes the Gamma function. In the Sec. III, we calculated the point estimation of  $\mathcal{T}_n^{(k)}$ . Therefore, in this part, we replace  $\mathbb{E}_q \left[ \mathcal{T}_n^{(k)} \right]$  with the point estimation of  $\mathcal{T}_n^{(k)}$ . Through analytical integration of all constituent terms and elimination of constant factors, we derive the following compact representation of the evidence lower bound (ELBO):

$$\begin{aligned}
ELBO = & -\frac{c^k}{2d^k} \mathbb{E}_q \left[ \left\| \mathcal{H}^k - \text{FCTN}(\mathcal{T}_1^k \times_1 \mathbf{P}_1, \mathcal{T}_2^k \times_2 \mathbf{P}_2, \mathcal{T}_3^k, \mathcal{T}_4^k) \right\|_F^2 \right] \\
& -\frac{e^k}{2f^k} \mathbb{E}_q \left[ \left\| \mathcal{M}^k - \text{FCTN}(\mathcal{T}_1^k, \mathcal{T}_2^k, \mathcal{T}_3^k \times_3 \mathbf{P}_3, \mathcal{T}_4^k) \right\|_F^2 \right] \\
& -\frac{1}{2} \sum_{n=1}^4 \text{Tr} \left\{ \mathbb{E}_q[\mathbf{\Lambda}_n^k] \left( \mathbf{T}_{n(n)}^k \top \mathbf{T}_{n(n)}^k \right) \right\} \\
& + \sum_{n_1=1}^3 \sum_{n_2=2}^4 \sum_r^{R_{n_1, n_2}} \left\{ \ln \Gamma(a_{n_1, n_2}^k) + a_{n_1, n_2}^k \left( 1 - \ln b_{n_1, n_2}^k - \frac{b_0^k}{b_{n_1, n_2}^k} \right) \right\} \\
& + \ln \Gamma(c^k) + c^k \left( 1 - \ln d^k - \frac{d_0^k}{d^k} \right) \\
& + \ln \Gamma(e^k) + e^k \left( 1 - \ln f^k - \frac{f_0^k}{f^k} \right) \\
& + C
\end{aligned}$$

In order to empirically verify the theoretical monotonicity property of our  $ELBO$  formulation, we performed a systematic convergence analysis on three benchmark datasets. It should be noted that the method is designed with group-independent inputs (each group is labeled as  $k$ ), so the convergence processes of different groups of  $k$  are independent of each other. Fig. 14 illustrate the  $ELBO$  trajectories under a consistent initialization scheme, in which all curves exhibit the guaranteed non-decreasing property, and the  $ELBO$  increases to stability within five iterations, which satisfies the general criteria for convergence, and further demonstrates the stability and convergence of BFCTN.

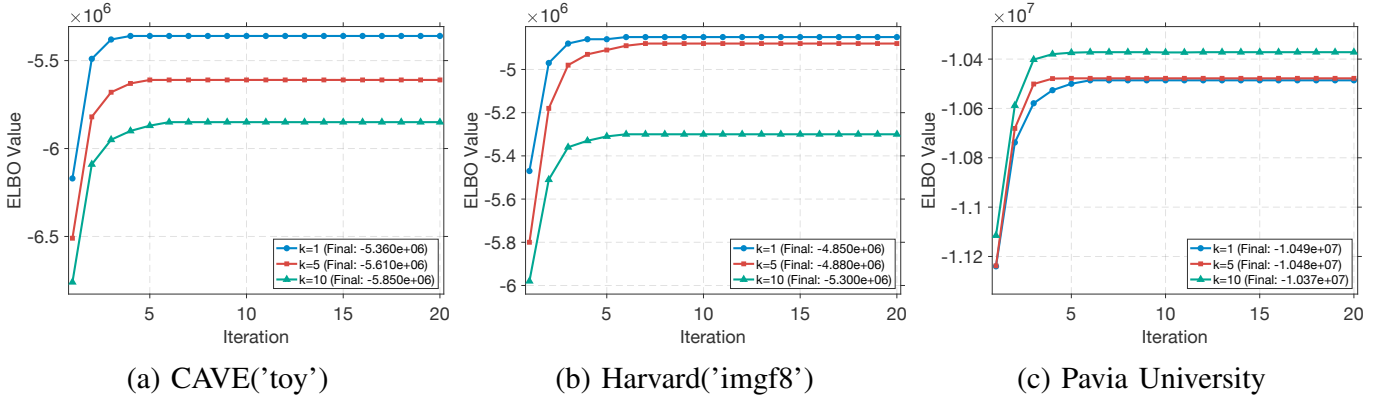


Fig. 14: The convergence of  $ELBO$  on three datasets.